Semi-Empirical Satellite Accommodation Model for Spherical and Randomly Tumbling Objects

Marcin D. Pilinski,* Brian M. Argrow,† and Scott E. Palo‡
University of Colorado at Boulder, Boulder, Colorado 80309
and
Bruce R. Bowman§
U.S. Air Force Space Command, Colorado Springs, Colorado 80309

Orbits of launch-vehicle upper stages and spheres were observed by U.S. Air Force Space Command, and the resulting observations were converted by the Space Analysis Office to fitted ballistic coefficients by comparing the observed orbit with an orbit predicted by an atmospheric-drag model. The ballistic coefficients contain signals that result from atmospheric variability not captured by the model as well as signals that correspond to changes in the satellite-drag coefficient. For objects in highly elliptical orbits with perigee altitudes below 200 km a 50% change in ballistic coefficient can be observed. This drastic change is associated with both changes in the energy accommodation coefficient driven by atomic-oxygen adsorption and entry into a transition flow region where a diffuse shock forms ahead of the satellite near perigee. Furthermore, the observed ballistic coefficients for objects in near-circular orbits (7.5 km/s speeds) do not match those of objects in highly eccentric orbits (10 km/s speeds near perigee). This difference is attributed to a decrease in adsorption efficiency postulated by previous researchers that is formalized in this work into a semi-empirical model. The model parameters suggest that the average binding energy of atomic oxygen on satellite surfaces is about 5.7 eV.

Nomenclature

A	=	projected area, m^2
a	=	aerodynamic acceleration, $m \cdot s^{-2}$
$\mathbf{a}$	=	aerodynamic-acceleration vector, $m \cdot s^{-2}$
B	=	inverse ballistic coefficient, $m^2 \cdot kg^{-1}$
b	=	ballistic coefficient, $kg \cdot m^2$
C	=	force-coefficient magnitude
CF	=	cost function
D	=	adsorption efficiency
d	=	cylinder diameter, m
E	=	kinetic energy, eV
F	=	wind factor
f	=	probability density function
I	=	modified Bessel function
$\hat{i}, \hat{j}, \hat{k}$	=	basis vectors of the Earth-centered-inertial reference frame where $\hat{k}$ is aligned with Earth's rotation axis
K	=	adsorption constant, $torr^{-1}$
k_B	=	Boltzmann constant, $m^2 \cdot kg \cdot s^{-2} \cdot K^{-1}$
l	=	cylinder length, m
m	=	mass, kg
n	=	atmospheric number density, m^{-3}
P	=	pressure, torr
R	=	distance from reference-frame origin to spacecraft position, m
$\mathbf{R}$	=	spacecraft-position vector, m
s	=	speed ratio
T	=	temperature, K
t	=	time, s
V	=	velocity magnitude, $m \cdot s^{-1}$
$\mathbf{V}$	=	velocity vector, $m \cdot s^{-1}$
$\hat{v}$	=	velocity unit vector, $m \cdot s^{-1}$
$\hat{x}, \hat{y}, \hat{z}$	=	basis vectors of the satellite body frame
Y	=	satellite observable quantity
α	=	energy accommodation coefficient
γ	=	most-probable speed, $\gamma = \psi^{-1}$, $m \cdot s^{-1}$
η	=	fraction of propellant remaining
θ	=	fractional coverage of adsorbate
θ'	=	effective coverage of adsorbate
μ	=	fraction of atmospheric-molecule to surface-molecule mass
ρ	=	atmospheric mass density, $kg \cdot m^{-3}$
ψ	=	inverse of most-probable speed, $s \cdot m^{-1}$
ω_e	=	Earth's rotation rate, 7.2921×10^{-5} $rad \cdot s^{-1}$

Subscript

A	=	component along the axis of symmetry
a	=	atmospheric
ads	=	adsorbate
b	=	chemical binding energy
cap	=	flat plates of cylindrical solid
cyl	=	cylinder
D	=	drag direction
dry	=	dry mass
e	=	Earth
eq	=	plane of the geographic equator
f	=	final
H	=	hydrogen
He	=	helium
i	=	observation index
in	=	incoming molecule properties
kin	=	kinetic
L	=	Langmuir
mod	=	modeled
N	=	component normal to axis of symmetry
N_2	=	molecular nitrogen

*Graduate Research Assistant, Department of Aerospace Engineering Sciences.

†Associate Fellow, Professor, Department of Aerospace Engineering Sciences; Director, Research and Engineering Center for Unmanned Vehicles.

‡Associate Professor, Department of Aerospace Engineering Sciences, Colorado Center for Astrodynamics Research, Research and Engineering Center for Unmanned Vehicles. Associate Fellow AIAA.

§Senior Astrodynamicist, Space Analysis/A9AC, Atrium II, Suite 212, 1150 Academy Park Loop.

O	=	atomic oxygen
o	=	initial
obs	=	observed coefficient and corrected for atmospheric bias
out	=	outgoing molecule properties
O_2	=	molecular oxygen
prop	=	propellant
q	=	species index
r	=	relative to atmospheric motion
s	=	surface material
sc	=	spacecraft
w	=	atmospheric wind
w	=	wall (spacecraft surface)
$x,$	=	the $\hat{x}$, $\hat{y}$, or $\hat{z}$ satellite-body-frame directions where x is in
y, z		the ram direction
Δt	=	averaging time span

I. Introduction

THE motivation for realistic modeling of satellite ballistic coefficients can be outlined in terms of two complimentary sets of objectives. The first is the operational capability to predict satellite orbits accurately for reentry specification and conjunction analysis between active satellites and orbit debris as well as many other engineering applications associated with the positioning of assets in low Earth orbit (LEO). The second is the scientific need to understand the climatology and short-term variability of Earth's thermosphere, which is supported in part by neutral density observations derived from satellite-drag measurements. For example, observations of rocket bodies [1] with very low perigee altitudes and highly eccentric orbits (orbit eccentricity $e > 0.2$) allow examination of atmospheric densities between 100-km and 200-km altitudes. However, to interpret such observations, a drag coefficient must be assumed. The perigee velocity of objects in highly eccentric orbits will be higher than those in near-circular orbits causing the kinetic energy of the gas colliding with the satellite surface to be correspondingly higher. It has long been suspected [2] that the gas-surface interactions (GSI) of atmospheric constituents with the satellite surface could be a function of the incident kinetic energy and that this change in GSI will alter the drag coefficient. Furthermore, gas-gas interactions such as the generation of a diffuse-shock region may no longer be neglected below 150-km altitudes [3] and must be considered in the computation of drag coefficients. Kinetic energy and the flow regime are not the only considerations in the computation of satellite drag. Atmospheric composition and the chemisorption of atomic oxygen also play important roles and cause an altitude-dependent change in the coefficient of drag [4–6]. The purpose of the present work is to develop a model of changes in satellite-drag coefficient as a function of atomic-oxygen adsorption, atmospheric composition, perigee velocity, and flow regime. This model will enable computations of satellite-body forces caused by interactions with Earth's atmosphere as well as the determination of densities through observations of such forces.

The primary relationship describing satellite drag (acceleration) as a function of density is described as:

$$\mathbf{a} = -\frac{1}{2} \cdot B \cdot \rho \cdot \|\mathbf{V}_{\text{sc}} - \mathbf{V}_w\|^2 (\hat{v}_r) \qquad (1)$$

$$\hat{v}_r = \frac{(\mathbf{V}_{\text{sc}} - \mathbf{V}_w)}{V_r} \qquad (2)$$

$$V_r = \|\mathbf{V}_{\text{sc}} - \mathbf{V}_w\| \qquad (3)$$

where $\mathbf{a}$ is the drag-acceleration vector, B is the inverse ballistic coefficient, ρ is the mass density, and $\mathbf{V}_w$ and $\mathbf{V}_{\text{sc}}$ are the atmospheric wind and the spacecraft velocity vectors, respectively. Equation 4 defines the inverse ballistic coefficient

$$B = b^{-1} = \frac{C_D A}{m_{\text{sc}}} \qquad (4)$$

where b is the ballistic coefficient, A is the projected area of the object, C_D is the unitless coefficient of drag, and m_{sc} is the spacecraft mass [7]. For brevity B will be referred to as the ballistic coefficient. The mass and cross-sectional area may be estimated a priori and assumed to be constant over the life of the orbit as long as the object does not break up or lose propellant. However, the drag coefficient is a function of many parameters, as mentioned in the preceeding paragraph, and cannot be assumed constant. These parameters include gas-surface interactions, satellite-surface contamination, and atmospheric composition [2].

At the beginning of the space age Cook [8] and Reiter and Moe [9] both suspected that adsorbed gas molecules such as atomic oxygen contaminate the satellite surface and may have a significant effect on the determination of drag and atmospheric densities. Later, the work of Moe et al. [2,6] was the first to demonstrate the importance of atomic oxygen in the determination of satellite-drag coefficient by showing that drag-force and drag-torque data cannot be explained by the assumption of uncontaminated surfaces and hard-sphere gas-surface models. As a result the energy accommodation coefficient that describes the level of inelastic behavior during a gas-surface collision was shown to be near unity at low altitudes and lower at higher altitudes. Pilinski et al. then integrated this information into a drag-coefficient model that accounts for the adsorption of atomic oxygen to satellite surfaces [4]. Whereas this previous model for energy accommodation coefficients was written as a function of partial pressure of atomic oxygen only, the model developed here will also take into account observed variations in the drag coefficient due to changes in incident kinetic energy. The pressure parameter will also be redefined such that changes in dynamic pressure caused by changes in satellite velocity are accounted for. The new model, called semi-empirical satellite accommodation model (SESAM), will include a number of added capabilities. First, the relationship between adsorption and accommodation is refined using a surface-weighted average of accommodation behavior in previously studied gas-surface regimes. Next, the model is extended to highly elliptical orbits by including the effect of kinetic energy on the sticking coefficient of atomic oxygen. The model development is based on results of accommodation measurements made using U.S. Air Force Space Command observations of rocket bodies and spheres in highly eccentric and circular orbits [1,10]. A comparison of the accommodation-coefficient model with existing data along with estimates of model accuracy is also presented.

II. Gas-Surface Interactions in Low Earth Orbit

There is strong evidence that the majority of gas-surface reflections are nearly diffuse up to 700-km altitude [6,11]. The assumption of a fully diffuse angular-reflection distribution allows an approximation of the gas-surface interaction by a single parameter called the accommodation coefficient α, which is a measure of the average fraction of energy lost by molecules impinging on the surface. The accommodation coefficient is defined by [12]

$$\alpha = \frac{T_{\text{kin,in}} - T_{\text{kin,out}}}{T_{\text{kin,in}} - T_w} \qquad (5)$$

where $T_{\text{kin,in}}$ is the kinetic temperature carried to the surface by an incoming molecule, $T_{\text{kin,out}}$ is the kinetic temperature of the reflected molecule, and T_w is the kinetic temperature the molecule would have if it was reemitted at the temperature of the surface.

A series of experiments and theoretical calculations [13–17] have shown that the heat of adsorption (binding energy) for atomic oxygen on various surfaces ranges from 1 to 10 eV putting it in the range of kinetic energies experienced by a spacecraft surface flying through an atmosphere primarily composed of atomic oxygen. As the spacecraft velocity changes from 7.6 to 10.2 km · s^{-1} in various orbits the average of the distribution of energies in the freestream moves from 4.8 to 8 eV. At higher energies a greater fraction of molecules may

have energies above binding, and this will undoubtedly effect the adsorption efficiency. A survey of literature [5,6,9,11,18–22] related to drag coefficients in LEO leads to the following general conclusions about the observed values of accommodation coefficients. First, accommodation is near unity near 200-km altitudes, and the reflected velocity distribution is nearly diffuse. As altitude increases (leading to lower atmospheric density) accommodation coefficients are reduced. Accommodation is also reduced with lower solar activity (lower atmospheric density). Finally, higher-incident kinetic energy (caused by high perigee velocities in orbits with appreciable eccentricity) is associated with lower accommodation coefficients. These observations are indicative of a strong relationship between atmospheric density and the accommodation coefficient, which has been explored in the previous model for satellites in circular orbits [4]. The available information also suggests a relationship between incident kinetic energy (orbit eccentricity) and the accommodation coefficient. In the development of the present model we consider a wider range of incident energies (eccentricities), apply a hard-sphere accommodation model to the fraction of surface not covered by adsorbate, and consider a measure of pressure (flux) that accounts for ram effects. We will assume that molecules will bond only to unoccupied sites, and the accommodation on a surface site depends on whether it is occupied or not. The overall or effective accommodation coefficient can then be described as a weighted average of the two GSI types provided that one makes the assumption of linear behavior with adsorbate coverage [23] according to

$$\alpha = (1 - \theta)\alpha_s + \theta\alpha_{\text{ads}} \tag{6}$$

In Eq. (6) θ represents the fraction of sites occupied by adsorbate, α_{ads} is the average accommodation coefficient experienced by incoming molecules colliding with the adsorbate, and α_s is the average accommodation coefficient for collisions with the surface material. The gas-substrate interaction can be simply approximated by a lattice interaction model such as that of Goodman [8,24]. In contrast, the choice for the interaction of a gas molecule with an adsorbed atom is not as clear. In this case one can be guided by empirical evidence suggesting that the effective accommodation in an oxygen-rich atmosphere is close to unity [5,6]. Furthermore, adsorption experiments involving adsorption at the gas-liquid interface provide further support for an α_{ads} value of unity when the impinging molecule is close in mass to the adsorbed molecule [25,26].

III. Drag-Coefficient Computations

In the free-molecular-flow regime (altitude greater than approximately 150 km) the drag coefficient may be computed by the use of integral equations. These are closed-form solutions that result from integrating the sum of the incoming momentum, generally based on a Maxwellian distribution, and the outgoing momentum, which is often based on the assumption of diffuse reflection with a choice of GSI model [27–29]. The integral equation for a sphere is [29]

$$C_{D,\text{sphere}} = \frac{2s^2 + 1}{\sqrt{\pi}s^3} \exp(-s^2) + \frac{4s^4 + 4s^2 - 1}{2s^4} \text{erf}(s)$$
$$+ \frac{2\sqrt{\pi}}{3s} \sqrt{T_{\text{kin,out}}/T_a} \tag{7}$$

where the speed ratio s is

$$s = |\mathbf{V}_r|\psi \tag{8}$$

and $\psi = \sqrt{m/(2k_B T_a)}$ and erf() denotes the error function defined as

$$\text{erf}(x) = \frac{2}{\sqrt{\pi}} \int_0^x \exp(-t^2) \, dt \tag{9}$$

Here temperature T_a refers to the thermal temperature of the ambient gas irrespective of its bulk motion [not to be confused with the

incident kinetic temperature in Eq. (10)]. The accommodation coefficient enters through the factor $\sqrt{T_{\text{kin,out}}/T_a}$. To solve for $T_{\text{kin,out}}$ one may substitute the equation for the incident temperature [Eq. (10)] into the expression for the energy accommodation [Eq. (5)].

$$T_{\text{kin,in}} = \frac{mV_r^2}{3k_B} \tag{10}$$

$$T_{\text{kin,out}} = \frac{m}{3k_B} V_r^2 (1 - \alpha) + \alpha T_w \tag{11}$$

Because this work is focused on the drag coefficients of spherical satellites and randomly tumbling rocket bodies, the integral equation for a cylinder is included in Sec. IX. A C_D solution such as that in Eq. (7) is evaluated separately for each of the primary constituents in the freestream. The results are then superimposed linearly via a weighted mean of partial mass densities [30,31].

In the case of complicated satellite geometries, such as the challenging minisatellite payload and Starshine satellites [30,32], a different approach must be taken to account for shadowing and multiple reflections from satellite surfaces. Test-particle codes account for shadowing and multiple reflections for drag computations in the free-molecular regime [30]. When the satellite altitude is low enough such that molecule-molecule interactions cannot be neglected direct-simulation-Monte-Carlo (DSMC) methods may be applied [3]. DSMC simulates molecule-molecule as well as molecule-surface collisions of arbitrary shapes by representing the flow of a statistical sample of molecules and choosing appropriate collision frequencies within that sample. The DSMC code used in this research is DS3V [33]. A variable-hard-spheres (VHS) model is specified within DSMC as the gas-gas collision model. Under VHS the diameter used to predict collision frequencies varies with the temperature of the gas. The variability is modeled according to a power law that has been empirically determined to match the observed gas viscosities [29]. The reference temperature and power-law exponent are set to 2880 K and 0.73, respectively. Molecule-specific settings are listed in Table 1 [3]. Included are the molecule diameter, rotational and vibration degrees of freedom (DOF), vibrational temperature, as well as rotational and vibrational relaxation numbers.

IV. Sensitivity Analysis to Model Assumptions

To simplify the modeling process as well as the inverse procedure of determining model parameters from observations we will use a sphere to approximate the drag coefficient of a randomly tumbling object. The error associated with this assumption does not exceed 2% as can be seen in Fig. 1 where the average C_D of a tumbling cylinder is compared with that of a sphere. The results in Fig. 1 were computed using integral equations in the free-molecular regime where the atmospheric temperature was 1100 K, the spacecraft-wall temperature was 350 K, the composition was 82% atomic oxygen and 18% molecular nitrogen, and the spacecraft velocity was 10 km · s⁻¹. The natural question that follows is whether or not the average is a good representation of central behavior of the drag coefficient for a tumbling object. To answer this question consider that the typical observed tumbling period of rocket bodies ranges from 1 to 15 s (60 to

Table 1 VHS parameter settings for modeling intermolecular collisions

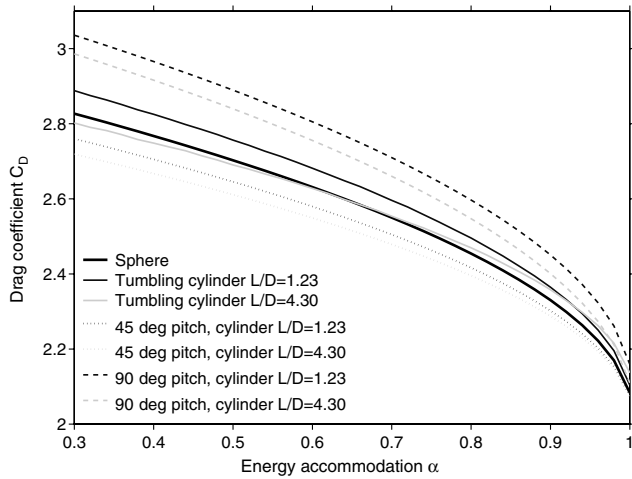| Molecule	Diameter, m	Rotational/ vibrational DOF	Vibrational temperature, K	Rotational/ vibrational relaxation numbers
O₂	3.06×10^{-10}	2/1	2270	5/50
N₂	3.08×10^{-10}	2/1	3390	5/50
O	2.30×10^{-10}	0/0	—	—/—

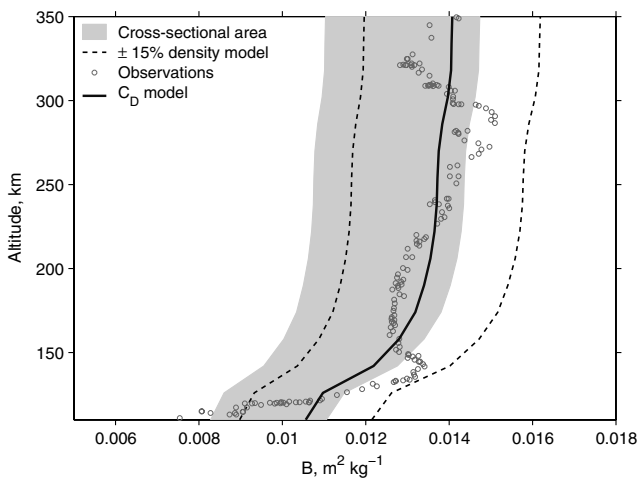Fig. 1 Drag coefficients of a sphere and randomly tumbling cylinders.

Fig. 2 Sensitivity of the ballistic coefficient of a rocket body.

4 rpm, respectively) [34–36]. Furthermore, the duration of a perigee pass (defined by the time spent within a single atmospheric scale-height of perigee) in low Earth orbit can range from from 2 to 90 min. Because the number of perigee passes during a 1.5-day orbit fit-span [37] may vary from 3 to 24 depending on orbit type, it follows that total perigee-pass times are approximately 6 to 2160 min (highly elliptical to near-circular orbits). In other words, the rocket bodies execute from 24 to 8,640 tumble periods (highly elliptical to near-circular orbits) during a single observation for the slowest tumbling objects and 360 to 129,600 for the most rapidly tumbling objects. The large number of expected revolutions that take place during a single drag measurement substantiate the use of average ballistic-coefficient properties.

The cross-sectional-area estimate can have a significant effect on the computation of a ballistic coefficient and on the computation of observed C_D from fitted ballistic coefficients. Fig. 2 demonstrates the relative size of cross-sectional-area uncertainty (gray region) compared with the modeled drag-coefficient variability (dark black) and uncertainty in atmospheric density (dotted lines). The plotted example is based on the Ariane rocket upper stage, which has the highest relative difference between minimum and maximum areas of all the objects in the dataset. Although the ballistic-coefficient variability due to cross-sectional area is much larger than that due to drag-coefficient effects, we nevertheless assume a constant average area and drag coefficient approximately equal to that of a sphere. This is because of the tumbling-rate argument presented in the preceding paragraph and because the ±15% (average) variability is observed to have a similar time-series for objects at approximately equal altitudes and orbital inclinations [38]. The latter observation indicates that

most of the short-term variability in fitted ballistic coefficients is due to errors in atmospheric density and not to large changes in cross-sectional area.

V.   Observations

Fitted ballistic coefficients have been computed by Bowman at U.S. Air Force Space Command Space Analysis Office [38] by comparing satellite-drag measurements to an atmospheric model and compensating for the differences between observed and modeled drag by adjusting the ballistic coefficient. It is important to understand that the fitted coefficients used in this analysis depend directly on the atmospheric model and indirectly on a priori assumptions about accommodation as a function of altitude. The reason for this dependence is that the biases in the density model are themselves estimated based on satellite-drag observations [10]. Model bias is estimated by comparing fitted drag coefficients with theoretical values that are based on existing knowledge of accommodation coefficients. Therefore, the resulting drag-coefficient and energy-accommodation values are not absolute and independent but are instead relative to the atmospheric model and the a priori assumptions of accommodation altitude profiles. The uncertainty in the fitted-accommodation results are estimated at approximately ±3%. For more information about atmospheric-model assumptions see work by Bowman and Moe [10] and Pilinski et al. [30]. Objects for which observed ballistic coefficients are available include spheres and rocket upper stages in a variety of orbits. Table 2 lists the rocket bodies (RB) and spheres (S) used in the present work. Original Department of Defense designators such as Soviet Launcher 6 (SL-6) are used throughout this paper. The data span several solar cycles from 1969 to early 2004. Rocket-body cross-sectional areas have been computed by averaging the projected area of an exact geometry model over many orientations generated from a distribution that corresponds to random tumbling. The geometry-model silhouettes can be seen in Fig. 3 with a 1-m marker shown for reference. Figure 4 shows the distribution of perigee sampling for all objects in the dataset. Note that the data covers altitudes from 110 to approximately 500 km. Latitude sampling is concentrated around the equator as well as 60 deg S due to the critical inclination of Molniya-class rocket bodies (SL-6 in Table 2). There are significant data at almost all local solar times with more samples in the afternoon.

Figure 5 illustrates an example of fitted ballistic coefficients along with two models. The data are from observations of two SL-8 (Kosmos) rocket bodies. Most of the periodicity is due to errors in the atmospheric model used to generate the fitted ballistic coefficients. Two sources of atmospheric-model error include the misrepresentation of the semiannual variation as a function of solar activity and the modeling of thermospheric heating from solar ultraviolet radiation [39]. Because the semi-annual variation is a temporal phenomenon, and the altitude of the satellites is decreasing with time, the periodic component appears to be a function of altitude. Two ballistic-coefficient models are also shown in Fig. 5. The first is SESAM, which is the subject of this paper. The second is a static ballistic-coefficient model in which B_{mod} is set equal to the average of the fitted ballistic coefficients over some initial time span in the dataset. This average-fixed value is assumed to be the true ballistic coefficient provided that the averaging time is sufficiently long and is a standard method of determining reference ballistic coefficients for density computations [7,40]. Notice that both the data and SESAM models deviate from the true value. As we will see, this deviation in B is a result of a decrease in drag coefficient caused partly by an increase in accommodation and partly by the shielding effect of reflected molecules in the transition regime.

Another source of drag-coefficient information is based on simultaneous measurements of density and energy accommodation. What makes these measurements unique is the measurement of two independent effects of the satellite-atmosphere interaction. This can be drag-torque and drag-force, drag-force and lift-force, or two measurements of drag made by satellites of distinct shapes (distinct drag coefficients) flying close together. A common method of implementing such measurements is the paddlewheel concept.

Table 2   Spheres and rocket bodies used in the determination of SESAM parameters

Name	Type	NORAD tracking number	Dry mass/propellant mass	Area	Surface
SL-3 (Vostok block-E 3rd stage)	RB	04120, 05143, 05328, 07418, 07969, 09854, 10135, 11056, 11156, 11269	820/2311 kg	7.825 m²	Al, paint
SL-8 (Kosmos 3M 2nd stage)	RB	05282, 22876	1435/18, 700 kg	10.76 m²	Al, paint
SL-6 (Molniya block-L 4th stage)	RB	11556, 12519, 16125, 19544, 20258, 20446, 03223, 14319, 15955, 15983, 16686, 16939	1160/5500 kg	8.328 m²	Al, Thermal-blanket
Ariane H10	RB	19332, 20042	1500/10, 800 kg	23.78 m²	Al
Ariane H10+	RB	23332	1630/11, 140 kg	24.20 m²	Al
Ariane H10-III	RB	23782, 23817, 24847, 25069, 25154, 25313, 25895, 26057, 26625	1770/11, 863 kg	24.28 m²	Al
Payload-assist-module (PAM) D	RB	13136, 17708, 20304, 20363, 21932, 22016, 22659, 24878, 25032, 26409	209.7/4431 kg	2.231 m²	Ti
Taifun-Yug	S	11796, 13750, 15446, 21190	750/ kg	3.142 m²	Al
Calsphere	S	04957, 04958, 04963	0.73/ kg	0.0507 m²	2 Al, 1 Au
4-in. Orbital Drag Environment RAdar Calibration Spheres (ODERACS)	S	22990, 22991, 23472	1.482/ kg	0.0081 m²	1 CrO_3, 1 Al, 1 paint
6-in. ODERACS	S	22994, 22995, 23471	5.0/ kg	0.0182 m²	1 CrO_3, 1 Al, 1 O_2
Starshine I	S	25769	39.46/ kg	0.193 m³	Al, SiO_2
Starshine II	S	26996	38.56/ kg	0.193 m³	Al, SiO_2
Starshine III	S	26929	90.04/ kg	0.701 m²	$Cr\ O_2\ SiO_2$
Sputnik 40	S	24958	2.270/ kg	0.0305 m²	Al
Sputnik 41	S	25533	2.330/ kg	0.0305 m²	Al
Sputnik 99	S	25685	4.830/ kg	0.0305 m²	Al

A description of this technique is made by Reiter and Moe [9] as well as Imbro et al. [20]. The satellite in their investigations is a major-axis spinner with the spin axis roughly aligned with the satellite velocity vector at perigee. This allows for a straightforward determination of drag torques because the drag-torque vector, due to the propeller-like geometry, is also aligned with the spin axis. Satellite drag is measured simultaneously through the observations of the satellite orbit.

Fig. 3   Rocket bodies from the fitted-ballistic dataset.
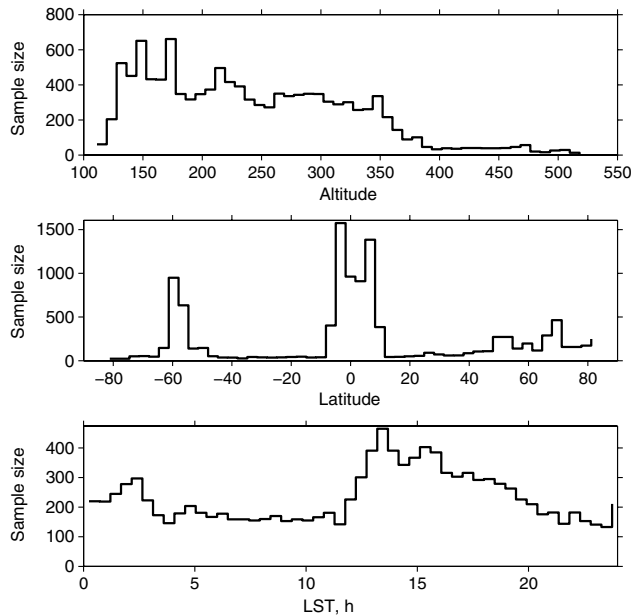
Fig. 4   Sample size organized by latitude, altitude, and local solar time (LST) bins.

The difference between the two estimates of density is minimized by varying the energy accommodation coefficient and GSI model. Paddlewheel data will be used to evaluate and fine tune the SESAM model.

VI.   Analysis Method

To obtain accommodation coefficients from fitted ballistic coefficients the data must first be multiplied by the assumed mass and divided by the cross-sectional-area estimate (see Table 2) to produce the observed drag coefficient $C_{D,\text{obs}}$. For spheres a priori information regarding area and mass is available. For rocket bodies a consistent procedure must be implemented to determine the mass. Liquid-fuel rocket boosters are highly optimized structures that can approach 80% propellant by mass [41]. A fuel margin (leftover propellant at burnout) of 10% in this case would mean a 29% increase in postburnout mass from the published dry mass. To estimate the true object mass the estimated GSI parameters for a rocket body are compared to those of a sphere flying through similar conditions (atomic-oxygen concentration and incident kinetic energy). We will return to the determination of mass later in this section.

Before analyzing the fitted-ballistic-coefficient data a number of auxiliary data products corresponding to each B_{obs} data point must be
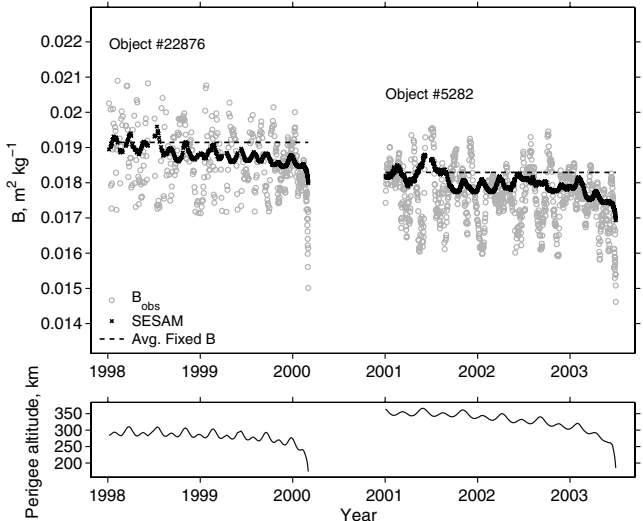

Fig. 5   SL-8 (Kosmos) $C_{D,\text{obs}}$ in the transition and free-molecular flow regimes.

generated. We begin by propagating each orbit using the general perturbations-orbit model SGP4 [42]. The orbit propagation was based on evolving orbital elements of each rocket body and sphere in Table 2, which were downloaded from CelesTrak¶ in the NORAD two-line element format. Next, the NRLMSISE-00 model is evaluated along the reference orbit to estimate parameters such as total atmospheric density and temperature. Effective properties corresponding to perigee measurements of B_{obs} are now obtained by computing the weighted average of property Y at measurement epoch t_i and observation time span of Δt. The computation of effective properties is described in Eq. (12) where the observation time span Δt is generally taken to be 1.5 days for consistency with the generation of fitted ballistic coefficients [37]

$$\langle Y(t_i)\rangle_{\Delta t} = \frac{\int_{t_i - \Delta t}^{t_i} Y(t)\rho_{\text{mod}}(t)C_{D,\text{est}}(t)V_{\text{sc}}(t)^3 F(t)\,\mathrm{d}t}{\int_{t_i - \Delta t}^{t_i} \rho_{\text{mod}}(t)C_{D,\text{est}}(t)V_{\text{sc}}(t)^3 F(t)\,\mathrm{d}t} \quad (12)$$

Note that in the preceding equation $\langle Y(t_i)\rangle_{\Delta t}$ is the effective property associated with measurement i, ρ_{mod} is the total mass density computed by NRLMSISE-00, V_{sc} is the spacecraft-velocity magnitude computed by SGP4, $C_{D,\text{est}}$ is the drag coefficient from Eq. (7) assuming $\alpha = 1.00$, and F is the wind factor [7] defined as

$$F = \frac{\|\mathbf{V}_{\text{sc}} - \mathbf{V}_w\|^2}{V_{\text{sc}}^3}[\hat{V}_r \cdot \mathbf{V}_{\text{sc}}] \quad (13)$$

which accounts for the reduction in drag due to a deviation of the relative wind direction from the spacecraft direction of flight. The wind vector $\mathbf{V}_w$ is computed based on a corotating atmosphere model in the following way

$$\mathbf{V}_w = \omega_e \hat{k} \times \mathbf{R}_{\text{eq}} \quad (14a)$$

$$\mathbf{R}_{\text{eq}} = R_x \hat{i} + R_y \hat{j} \quad (14b)$$

where $\hat{i}, \hat{j}, \hat{k}$ are unit vectors corresponding to the three basis vectors of the Earth-centered Earth-fixed coordinate frame, R_x and R_y are the x and y components of satellite position (computed with SGP4), and ω_e is the average rotation rate of the earth [43]. Note that the weighting factor inside the integrals of Eq. (12) can be thought of as the energy dissipated by aerodynamic drag along the satellite orbit. This is because the integral of $\rho^M(t)C_{D,\text{est}}(t)V_{\text{sc}}(t)^3 F(t)\,\mathrm{d}t$ is equivalent to the integral of $\rho^M(t)C_{D,\text{est}}(t)V_{\text{sc}}(t)^2 F(t)\,\mathrm{d}l$ where $\mathrm{d}l = V_{\text{sc}}(t)\,\mathrm{d}t$ is a differential arc length along the orbit. This formulation is equivalent to that used by Picone and Emmert to deduce effective atmospheric densities from NORAD two-line elements [7] except that here we do not remove the drag coefficient from inside the integral. The drag coefficient remains inside the integral in Eq. (12) due to the high-apogee altitudes experienced by some of the reference objects in our dataset. Accordingly, some satellites move regularly between an oxygen-rich atmosphere and one that is dominated by lighter species such as helium and hydrogen within a single orbit causing the drag coefficient to change drastically.

There are three effective properties that lie at the heart of parameterizing the SESAM model. The first is the estimated partial pressure of atomic oxygen (P_O in Eq. (15), which is computed along the orbit based on outputs of the NRLMSISE-00 atmospheric model

$$P_O = \frac{1}{2}\rho_O V_r^2 \left(\frac{2s^2+1}{\sqrt{\pi}s^3}\exp(-s^2) + \frac{4s^4+4s^2+1}{2s^4}\mathrm{erf}(s)\right) \quad (15)$$

In the preceding equation ρ_O is the mass density of oxygen that is equal to the number density n_O as reported by NRLMSISE-00 multiplied by $m_O = 2.656 \times 10^{-26}$ kg. The derivation of this pressure parameter is given in Sec. IX. The second effective parameter is the effective velocity V_r Eq. (3), which is used to compute the

incident kinetic energy of atomic oxygen ($E_r = 1/2 m_O V_r^2$). Finally, the mean molecular mass $\bar{m}$ is computed along the reference orbit based on NRLMSISE-00 composition values

$$\bar{m} = \frac{n_H m_H + n_{He} m_{He} + \ldots + n_{O_2} m_{O_2}}{n_H + n_{He} + \ldots + n_{O_2}} \quad (16)$$

All three parameters are mapped to a fitted-ballistic observation through Eq. (12).

To assess energy accommodation from fitted drag coefficients it is necessary to first generate a mapping from C_D to α. This is done via lookup tables generated by DSMC runs at various values of accommodation coefficient. DSMC computations of a sphere are made between 120- and 300-km altitudes (for example see Fig. 6). As discussed in the preceding section, this allows for the treatment of data from the transition regime. Figure 6 shows an example of a DSMC-simulated flowfield at 120 km. For altitudes below 120 km the model is linearly extrapolated, whereas above 300 km Eq. (7) is used. The 120-km lower limit was imposed because the vast majority of data exists above this altitude (see Fig. 4). The lookup values are shown in Fig. 7. After $C_{D,\text{obs}}$ profiles are computed for all objects in Table 2 they are inverted to form solutions of effective-energy-accommodation parameters. To do this a modeled drag coefficient is computed and compared with the observations. The modeled drag coefficient is based on a Langmuir isotherm generated by adjusting the Langmuir parameter K_L for each type of object at several kinetic-energy bins. The isotherm constitutes the forward model in our inversion, which will later become the basis of SESAM. Therefore, our objective is to determine the functional relationship of K_L that best fits the available drag-coefficient data. In previous work by
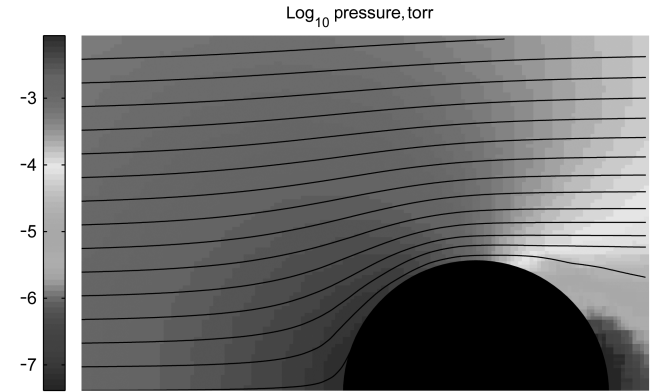

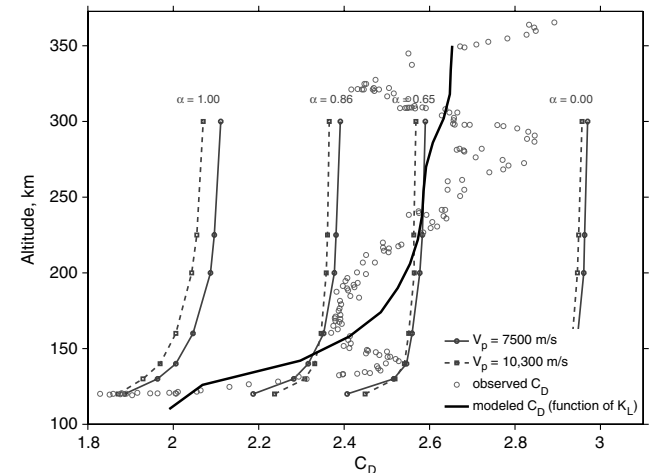**Fig. 6 DSMC simulation of a sphere at 120-km perigee altitude.**

Fig. 7 Theoretical C_D curves, empirical fit, and data for the SL-6 rocket body (15955).

¶Data available online at http://www.celestrak.com/ [retrieved 11 July 2011].

Pilinski et al. [4] a possible relationship between Langmuir isotherms and accommodation is introduced, which we will now exploit with a few modifications. This relationship begins by expressing the effective fractional coverage of atomic oxygen θ' as a function of the partial pressure of atomic oxygen

$$\theta' = \frac{K_L(E)P_O}{1 + K_L(E)P_O} \tag{17}$$

Note that we assume the Langmuir parameter $K_L(E)$ is a function of kinetic energy only. Next, the coverage parameter is converted to accommodation by assuming the accommodation on adsorbed surface sites α_{ads} is unity and rewriting Eq. (6) in the following way:

$$\alpha = (1 - \theta')\alpha_s + \theta' \tag{18}$$

In Eq. (18) α_s is computed by averaging Goodman's empirical equation [24] over a half sphere. The result is shown in Eq. (19)

$$\alpha_s = \frac{2.4\mu}{(1 + \mu)^2} \tag{19}$$

where μ is the ratio of incoming average molecular mass $\bar{m}$ to surface molecule mass m_s:

$$\mu = \frac{\bar{m}}{m_s} \tag{20}$$

We use an average surface-mass value of 65 atomic mass units (amu) for all objects in the dataset to simplify the computations. This number is near the average surface mass published by Moe et al. for spacecraft materials [6]. The effect of this choice is discussed in a later section.

The resulting accommodation coefficient α is then used as a lookup parameter in the DSMC C_D tables (illustrated in Fig. 7) or in the computation of $T_{kin,out}$ in the integral equation for a drag coefficient of a sphere Eq. (7). Recall that the integral equation is only applied when the data altitude exceeds the maximum tabulated altitude. The resulting drag coefficient will be referred to as $C_{D,mod}$ and can now be compared with $C_{D,obs}$ in the following way:

$$CF = \sum_{i=1}^{N_{obs}} (C_{D,obs,i} - C_{D,mod,i})^2 \tag{21}$$

The cost function CF described by Eq. (21) is computed for the number of available data points N_{obs} for a particular satellite and a range of incident kinetic energies. The value of $K_L(E)$ in Eq. (17) is chosen to minimize the cost function. The result of the inversion procedure and the lookup table values on which the fit is based are shown in Fig. 7.

Processing all observed data in the manner described in the preceding paragraph results in a series of Langmuir parameters $[K_L(E)]$ binned by kinetic-energy values. The functional relationship of $K_L(E)$ is assumed to have the following form:

$$K_L(E) = s_o(E, E_b, T_a)K_{L,o} + K_{L,f} \tag{22}$$

Equation 22 describes a transition from an initial Langmuir parameter associated with velocities in circular orbits $K_{L,o}$ to a final value $K_{L,f}$ associated with highly eccentric orbits. This transition is driven by an adsorption variable called the initial sticking coefficient or s_o [44]. A simple model for s_o is that any molecule with an incident kinetic energy exceeding the adsorption binding energy will not adsorb to the surface. To assess this quantity we first write the Maxwellian velocity distribution function $f(\mathbf{v})$ of incident molecules according to [29]

$$f(\mathbf{v}) = \frac{n_O}{(\pi\gamma^2)^{3/2}}\exp\left(-\frac{(\mathbf{v} - \mathbf{V}_r)\cdot(\mathbf{v} - \mathbf{V}_r)}{\gamma^2}\right) \tag{23}$$

where $\gamma = \psi^{-1}$, and n_O is the number density of atomic oxygen. To simplify the estimation of molecular kinetic energy we will assume that the in-track (defined as the x-direction) components of v and V_r are significantly larger than the thermal and off-track components ($v_x \gg v_y$, $v_x \gg v_z$, and $V_r \approx V_{r,x}$). Writing γ explicitly in the exponential function Eq. (23) now becomes

$$f(v_x) = \frac{n_O}{(\pi\gamma^2)^{3/2}}\exp\left(-\frac{m_O(v_x - V_r)^2}{2k_BT_a}\right) \tag{24}$$

Note that in Eq. (24) the mass of atomic oxygen is used as it is the primary adsorbent in this model. Now the $(-1/2)m(v_x - V_r)^2$ is expanded into $(1/2)m(-V_r^2 + 2V_rv_x - v_x^2)$ and rewritten into the form $-(1/2)mV_r^2 + 2\sqrt{m/2}V_r\sqrt{m/2}v_x - (1/2)m(-v_x^2)$. Using the definition of kinetic energy $[E = (1/2)mv^2]$ Eq. (24) is rewritten as Eq. (25)

$$f(E) = \frac{n_O}{(\pi\gamma^2)^{3/2}}\exp\left(\frac{-E_r + 2\sqrt{E_rE_x} - E_x}{k_BT_a}\right) \tag{25}$$

It is now time to implement the assumption that an impinging atomic-oxygen atom is only adsorbed if its ram-direction kinetic energy E_r does not exceed the adsorption or binding energy E_b. Accordingly, the initial sticking coefficient s_o can be defined as the normalized fraction of the energy distribution that falls below the adsorption energy [Eq. (26a)]

$$s_o = \frac{\int_0^{E_b} D(E)f(E)\,dE}{\int_0^\infty D(E)f(E)\,dE} \tag{26a}$$

In Eq. (26a) $D(E)$ is a measure of the efficiency of adsorption at any given energy and is associated with phenomena such as tunneling or other intrinsic changes in GSI [16,23,45]. Assuming $D(E) = 1$ then performing the integration results in Eq. (26b)

$$s_o = \left\{\sqrt{\pi k_BT_aE_r}\left[\text{erf}\left(\frac{\sqrt{E_b} - \sqrt{E_r}}{\sqrt{k_BT_a}}\right) + \text{erf}\left(\sqrt{\frac{E_r}{k_BT_a}}\right)\right]\right.$$
$$+ k_BT_a\exp\left(-\frac{E_b + E_r}{k_BT_a}\right)\left[\exp\left(\frac{E_b}{k_BT_a}\right) - \exp\left(\frac{2\sqrt{E_bE_r}}{k_BT_a}\right)\right]\right\}$$
$$\cdot\left\{\sqrt{\pi k_BT_aE_r}\left[\text{erf}\left(\sqrt{\frac{E_r}{k_BT_a}}\right) + 1\right] + k_BT_a\exp\left(-\frac{E_r}{k_BT_a}\right)\right\}^{-1} \tag{26b}$$

The concept described in Eq. (26b) is visually demonstrated in Fig. 8. Note that the sticking coefficient goes to unity far below the binding
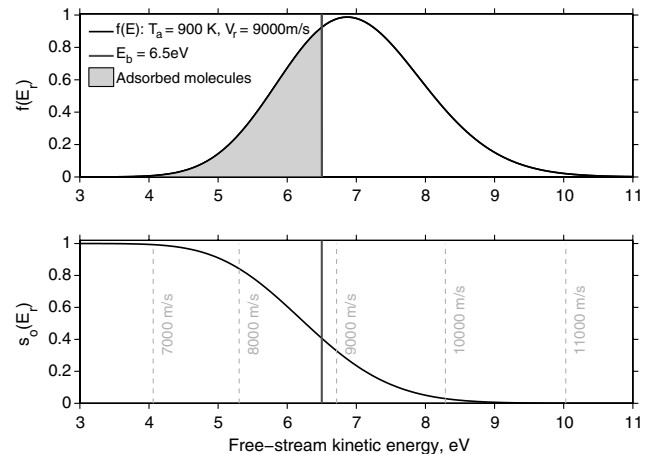

Fig. 8 Changes in initial sticking coefficient as a function of the binding energy.
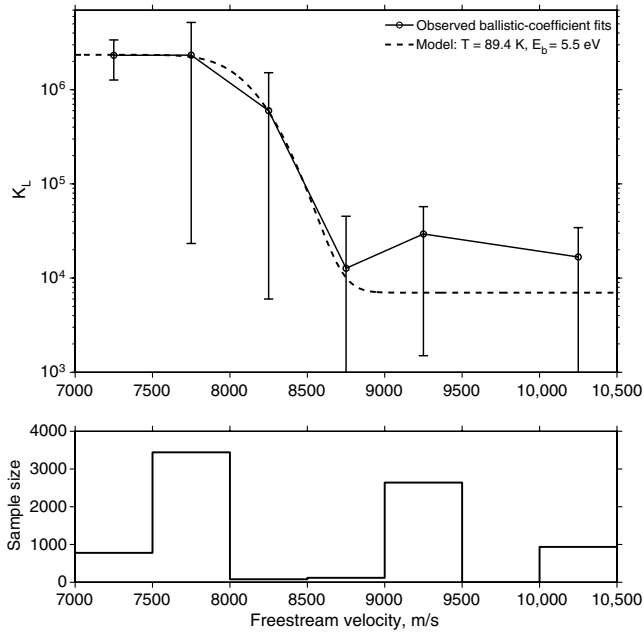
563

Fig. 9 Changes in the Langmuir parameter with energy assuming 2% propellant mass.

Fig. 10 Changes in the Langmuir parameter with energy assuming derived propellant mass.

energy and to zero when the average kinetic energy significantly exceeds E_b.

Now the functional relationship between Langmuir parameters and kinetic energy can be leveraged to fit the binned $K_L(E)$ data. A nonlinear least-squares fit is employed, which results in estimates of $K_{L,o}$, $K_{L,f}$, E_b, and T_a. For rocket bodies the fit parameters are a function of the assumed mass, and several iterations of data fits are performed, each with a different assumption for the mass of the spacecraft. Spacecraft mass is adjusted by modifying the propellant margin as shown in Eq. (27)

$$m_{sc} = m_{dry} + \eta_{prop} m_{prop} \qquad (27)$$

where m_{dry} and m_{prop} are the masses of the rocket body without propellant and the mass of the propellant (see Table 2), respectively, whereas η_{prop} is the propellant margin remaining after the final engine burn. For each rocket body a value of η_{prop} is chosen such that the $K_{L,o}$ resulting from the nonlinear fit is equal to the average $K_{L,o}$ value for all spherical rocket bodies (5×10^6). Thus, we avoid the need to assume an arbitrary value of accommodation coefficient at a certain altitude, atomic-oxygen partial pressure, or velocity to fix rocket-body masses. Note that the propellant margin should be a positive near-zero fraction (for an optimized launch). In practice the estimated η_{prop} may contain errors in the estimated cross-sectional area causing it to be slightly negative. Nevertheless, a benefit of this method is that it allows for a quality check of the resulting model-parameter fits.

VII.   Initial Model-Parameter Results

To adequately constrain the least-squares fit of Langmuir parameters it is necessary to assume the high-velocity value of the Langmuir parameter $K_{L,f}$. This value was initially fixed according to the data beyond 9000-m/s velocities equal to 7×10^3. Figure 9 shows the results of binned Langmuir-parameter fits under the assumption of a constant 2% propellant-mass margin for all rocket bodies. The bottom of the plot indicates the number of samples (fitted ballistic coefficients) in each kinetic-energy bin.

Note how the Langmuir parameter is reduced with incident kinetic energy indicating that adsorption is less efficient at higher velocities. Now K_L values are analyzed with rocket-body masses adjusted such that the resulting $K_{L,o}$ is consistent with that of spheres flying under similar atmospheric conditions (as described in the preceding section). The data and fit are shown in Fig. 10. The sample size in each bin has changed because outlier rejection is applied before
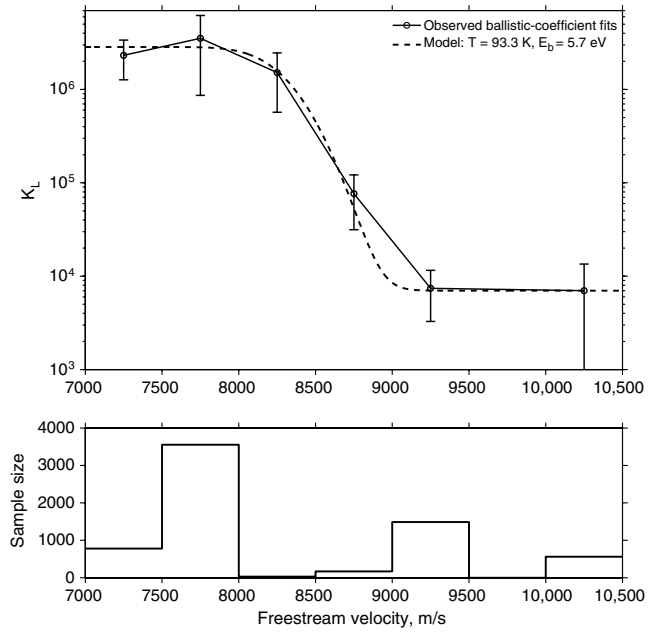
fitting the data, and the exact distribution of K_L values differs based on the assumed mass of the rocket bodies. This second fit is also indicative of a reduction in adsorption efficiency at higher velocities. Furthermore, the standard deviation (indicated by error bars) is reduced significantly by applying the mass-determination method. The fit parameters are $5.5 < E_b < 5.7$ eV, $89 < T_a < 93$ K, and $1.2 \times 10^6 < K_{L,o} < 2.0 \times 10^6$. The adsorption, or binding, energy resulting from the orbit-data fit is within a range of theoretical and laboratory results on various surfaces as seen in Table 3. Note that the average binding energy for the materials in Table 3 is 4.3 eV.

However, the atmospheric temperature T_a that has to be assumed for the incident Maxwellian distribution is clearly unphysical as the perigee altitudes vary from 110 to 500 km where temperatures should range from 200 to 1400 K. A low temperature in our fit (less than 100 K) accounts for the steep initial drop in K_L as a function of kinetic energy and is likely indicative of additional physics missing from the model. This could be empirically addressed by either choosing a nonconstant adsorption-efficiency function $D(E)$ or simply by recognizing that T_a in Eq. (26b) does not correspond to atmospheric temperature. From now on the transition-width parameter in Eq. (26b) will be referred to as T_{ad}. This could include sputtering or tunneling phenomena or a change in the surface properties with the level of adsorbate coverage θ.

VIII.   Model Evaluation and Tuning

The current method of determining Langmuir parameters introduces fuel-margin dependence into the determination of $K_{L,o}$ as indicated by the differences between Figs. 9 and 10. However, spherical satellites whose masses are known may be used to constrain the low-velocity Langmuir parameter. Figure 11 shows the average observed drag coefficients of all spherical objects in Table 2 as a

Table 3   Laboratory and theoretical results for the surface-binding energies for atomic oxygen

Surface	E_B, eV	Reference
Si 100	3.4	[13]
Al 111	7.6	[14]
Kapton	1.5	[17]
Fe 110/100	1.5–3.4	[16,46]
Graphite	11.2	[15]
Au 111	2.2–3.7	[47]

function of atomic-oxygen partial pressure. Also shown is the SESAM-model drag coefficient under three assumptions for $K_{L,o}$ as well as results of several other models. The first model is based on Eq. (7) with the energy accommodation coefficient fixed at several values. The second model is also based on Eq. (7) with the accommodation coefficient based entirely on the Goodman model [Eq. (19)]. The C_D comparisons in Fig. 11 indicate that the SESAM with $K_{L,o} = 5 \times 10^6$ outperforms both the Goodman and fixed-accommodation models. The vertical grey lines indicate reference altitudes for the pressure coordinates.

The sphere data can be further leveraged to examine SESAM performance as a function of surface mass m_s assumptions. One can compare observed drag coefficients of only those spherical satellites whose surface material is both known and homogeneous over the surface of the sphere. Figure 12 shows the effect of various surface masses on drag coefficient for a range of atomic-oxygen partial pressures. There appears to be no statistically significant difference between the drag coefficients of objects having different surface masses below 500-km altitude. The possible exception is gold
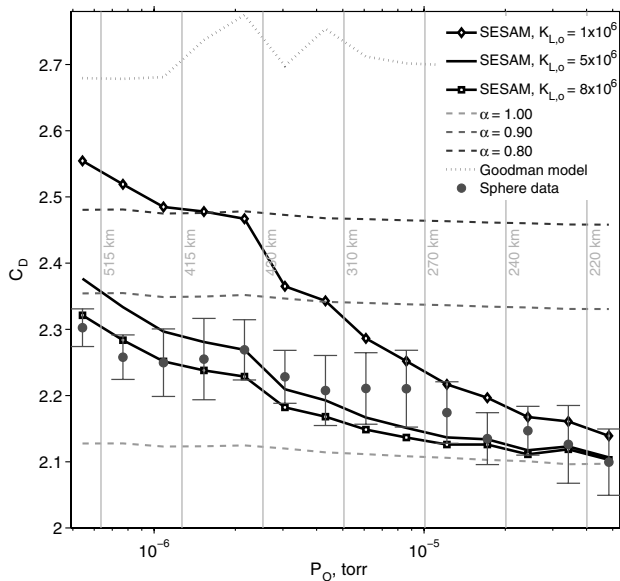

Fig. 11   Observed drag coefficients of spherical satellites compared to various models.
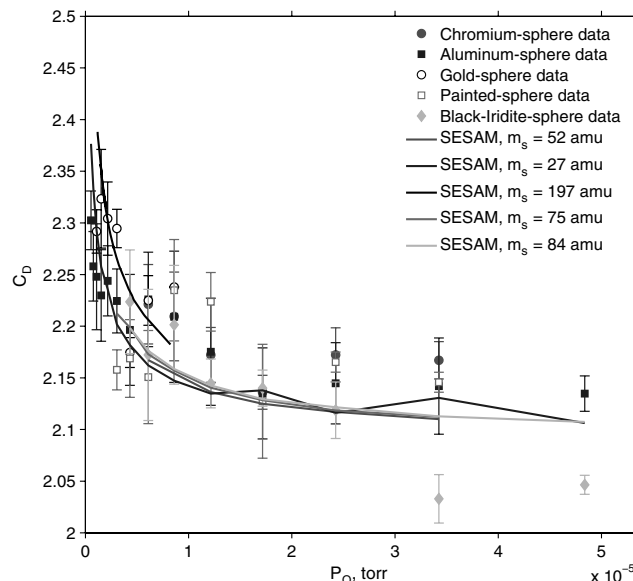

Fig. 12   SESAM with $K_{L,o} = 5 \times 10^6$ compared with sphere data of different surface compositions.

($m_s = 197$ amu), which seems to cause a drag coefficient that is approximately 2% higher compared to aluminum ($m_s = 27$ amu) at low oxygen pressures. The SESAM model does reproduce this difference, which can be attributed to the higher fraction of the Goodman accommodation model mixing at higher altitudes (470 to 520 km). These findings are consistent with the results of Moe and Bowman who also concluded that the effects of surface properties on the drag coefficient of spheres is negligible [10,22]. Therefore, setting the SESAM-model surface mass to a rather arbitrary value such as 65 amu seems to have little effect below an altitude of 500 km.

In addition to the fixed-accommodation and Goodman models it is also instructive to compare SESAM to a fixed-ballistic-coefficient model. This is because several derivations of atmospheric density from satellite drag such as the high-accuracy satellite-drag model [40] or the long-term density dataset [48] assume a true ballistic coefficient equal to the average fitted value over the beginning of the object lifetime. In the context of atmospheric-density measurement the ratio of the fitted to true (or in our case modeled) ballistic coefficients is equal to the ratio of observed to modeled density [7]. Therefore, the ratio of observed to modeled coefficients will be evaluated for four models (SESAM, Goodman, fixed-accommodation, and fixed average ballistic coefficient). Because the observed and modeled atmospheric densities can be approximated by normally distributed random variables, the ratio of B_{obs} to B_{mod} (ΔB) should result in a Cauchy distribution. Errors in the modeled ballistic coefficient will result in a distortion of the distribution. For the three physical models (SESAM, Goodman, and fixed accommodation) the initial (2-month) average ballistic coefficient will be compared to the modeled drag coefficient for each body to determine the mass margin appropriate for each rocket body. In the case of spheres the published mass will be used. The B_{obs}/B_{mod} result can be seen in Fig. 13, and the associated mass margins are shown in Fig. 14. In Fig. 14 black lines indicate the maxima and minima of the distributions, the blue box extends from the bottom 25th percentile to the top 75th percentile of the distribution, and the red line represents the median. The values of ΔB 10% trimmed-mean $\mu_{10\%,\Delta B}$, median $\mu_{1/2,\Delta B}$, standard deviation $\sigma_{\Delta B}$, and rms difference between ΔB and the Cauchy distribution are shown in the plot. The zero-mean Cauchy distribution is plotted in grey in each panel. SESAM outperforms the other physical models in terms of proximity of mean and median and rms difference from the reference distribution. In terms of unity mean only the fixed-accommodation model is comparable. Also, SESAM performs at least as well or better than the average-fixed-ballistic-coefficient model with the exception of standard deviation, which is 10% higher for SESAM. Meanwhile, the Goodman model results in a bimodal distribution, which is probably a result of better performance for rocket bodies with large perigee velocities (lower accommodation) and poor performance for rocket bodies and spheres with smaller values of perigee velocity (higher accommodation). The fixed-accommodation model results in reasonable values of mean (1% from unity) and standard deviation (10%) though it does appear to be skew symmetric. However, examining the resulting propellant margins for the physical C_D models reveals a significant distribution of negative values associated with fitting to the fixed-accommodation model (see Fig. 14). This unphysical result eliminates the fixed-accommodation model as a viable choice for drag analysis at multiple altitudes and satellite velocities. The Goodman model fares better though resulting propellant margins can be as high as 7%. The Goodman model results may be arbitrarily helped by adopting relatively high propellant margins (Fig. 14) and that the model is disqualified from direct application to LEO satellites by the comparison with sphere data (Fig. 11). Propellant margins resulting from fits to the SESAM model are near zero and primarily positive. Some slightly negative propellant margins may be due to errors in cross-sectional-area determination. Given the results in Figs. 13 and 14 the SESAM model is thus far the only physical C_D model capable of producing reasonable propellant margins as well as B_{obs}/B_{mod} distributions that are comparable to the average-fixed-ballistic-coefficient method.

The altitude dependence of B_{obs}/B_{mod} is shown in Fig. 15. The outstanding feature of the altitude-based comparison is the reduction in observed-versus-modeled coefficients below 200-km altitude.
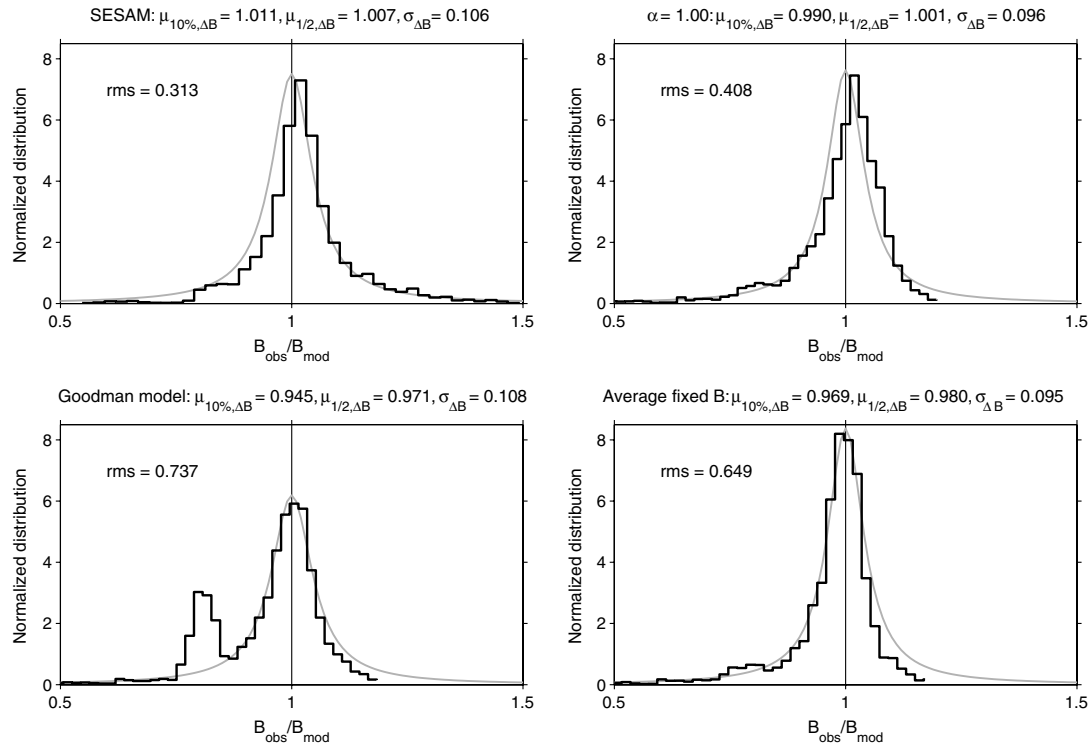
SESAM: $\mu_{10\%,\Delta B} = 1.011, \mu_{1/2,\Delta B} = 1.007, \sigma_{\Delta B} = 0.106$

$\alpha = 1.00$: $\mu_{10\%,\Delta B} = 0.990, \mu_{1/2,\Delta B} = 1.001, \sigma_{\Delta B} = 0.096$

Goodman model: $\mu_{10\%,\Delta B} = 0.945, \mu_{1/2,\Delta B} = 0.971, \sigma_{\Delta B} = 0.108$

Average fixed B: $\mu_{10\%,\Delta B} = 0.969, \mu_{1/2,\Delta B} = 0.980, \sigma_{\Delta B} = 0.095$

Fig. 13   Ratios of observed and modeled ballistic coefficients for the entire dataset.
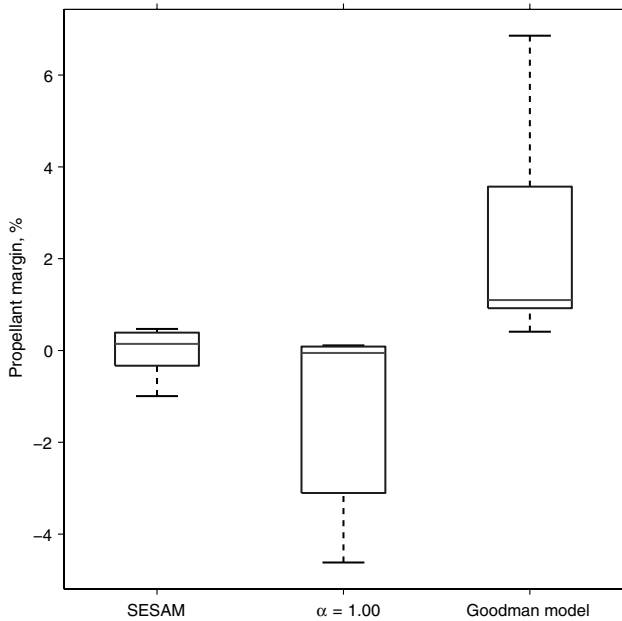
Fig. 14   Distribution of rocket-body fuel margins for three different ballistic-coefficient models.

Fig. 15   Ratios of observed and modeled ballistic coefficients binned by altitude.

Much of this reduction is associated with transition aerodynamics that reduce C_D. This can be seen most directly in the average-fixed model case, which begins to deviate at 170-km altitudes and results in almost 50% bias at 110-km altitudes. This bias will map directly into determination of density from such measurements and results from the fact that true ballistic coefficients are fixed in the free-molecular regime for the average-fixed model. Above 200 km the SESAM model matches the average-fixed model most closely whereas below 200 km SESAM does not result in significant altitude-dependent bias until approximately 125-km altitude with the maximum bias being 20% near 110 km. As discussed in preceding sections the measurement of B_{obs}/B_{mod} is indicative of atmospheric-density variation
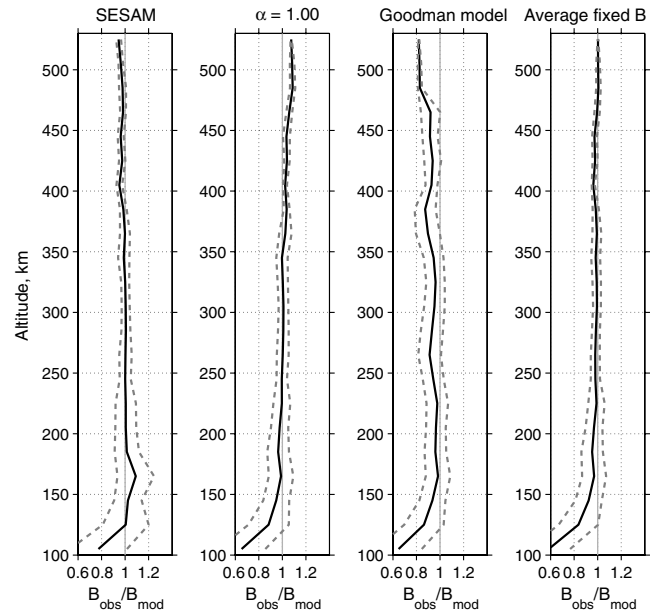
from a reference model. Therefore, altitude-dependent biases in Fig. 15 can also result from errors in total atmospheric density. To evaluate this possibility the ratio of observed to modeled ballistic coefficients is compared with the ratio of observed to modeled densities as measured by the Global UltraViolet Imager (GUVI) instrument [49,50]. The GUVI instrument is part of the Thermosphere Ionosphere Mesosphere Energetics and Dynamics (TIMED) mission launched into a 74.1-deg inclination 625-km circular orbit in December 2001. The objectives of the TIMED mission are to characterize the density, temperature, and winds between 60 and 180 km. A technical description of the instrument design is given by Paxton [49]. The instrument is designed to take spectra of the far

ultraviolet dayglow, which, while limb scanning, provides signatures of major thermospheric species O, N_2, and O_2. Spectral bands observed by the instrument are excited by photoelectron ionization or ionization via precipitating solar particles. Photoelectrons are formed in the upper atmosphere when atmospheric gases are ionized by solar radiation with wavelengths less than 40 nm. Although emission in several bands corresponds to concentrations of the emitters, O and N_2, molecular oxygen is inferred through the molecular-absorption of radiation. The tangent altitudes of the GUVI limb scans range from 110 to 520 km. The level-two data include geolocated products such as densities and temperatures as well as their uncertainties mapped to the geographic location.[**] The instrument produces approximately 390 limb scans per orbit covering a range of latitudes and providing ample opportunity for comparisons with our drag dataset.

The inversion used to determine the concentrations of O, N_2, and O_2 from dayglow is of the maximum-likelihood type using NRLMSIS-00 as the forward model for concentration. The first step is the prediction of intensities of certain Far UltraViolet (FUV) bands using the forward model. These are then compared to measured intensities. Model parameters are next adjusted to bring the modeled and observed intensities into agreement while producing the solution for concentration values. Because of the use of NRLMSISE profiles in the inversion, the process also results in the estimation of thermospheric temperatures. Although the observed emissions are simple processes, uncertainties become large at high solar-zenith angles (near noon local solar time) where multiple scattering and self-absorption of the dayglow photoelectrons may become significant. Accordingly, the GUVI limb inversions are limited to a solar-zenith angle of less than 80 deg, which causes periodic temporal gaps in the density data. A g-factor, which describes the excitation rate (per second per molecule), is also simulated in the forward model as an altitude profile calculated based on the integrated column concentration of O, N_2, and O_2 between the inversion location and the sun. This and other details about the inversion process are described in a paper by Meier and Picone [51]. The g-factor is multiplied by the modeled molecular concentration and integrated along the line of sight to the instrument to predict the total emission. Tangent altitudes above 300 km are not used in the inversion because the g-factor model (chosen for efficiency) does not apply above this altitude. However, due to the use of the NRLMSISE-00 model in the density-forward model, densities are easily extrapolated to higher altitudes. The NRLMSISE model is scaled using four linear parameters. Parameter f_{N2}, f_{O2}, and f_O independently scale the number densities inside NRLMSISE, whereas f_{10} scales the 10.7-cm-wavelength flux input. The resulting number density for species q based on GUVI observations is computed as shown in Eq. (28)

$$n_q^{\text{GUVI}} = f_x \times n_q^{\text{MSIS}}(f_{10} \times F10.7P, f_{10} \times F10.7A) \qquad (28)$$

$F10.7P$ and $F10.7A$ indicate the measured values of the 10.7-cm solar-radio flux on the previous day and the 81-day average, respectively. A distinct feature of this method is that the solutions for concentrations do not depend on absolute instrument calibration because the important information is contained in the shapes of the altitude profiles of emission rates. The inversion 1-σ precision can vary from $\pm 5\%$ during solar maximum to $\pm 20\%$ during solar minimum. Because O, N_2, and O_2 comprise the majority of the atmosphere below 400 km, it is possible to sum their mass contribution and compare the product with total mass density derived from satellite drag. Emmert et al. compared GUVI data with global densities derived from a large set of orbiting bodies with perigees at altitudes ranging from 200 to 600 km [50].

Because GUVI limb scans produce total-density data only during daytime (but not near noon), the drag data are binned to restrict local time accordingly. The data are also separated into low-geographic latitude (−11.5 to 11.5 deg) and high latitude (−65 to −55 deg) in both datasets. The time-span is restricted to include data from 2001 and 2002 and exclude 2003 and 2004 where the comparison between
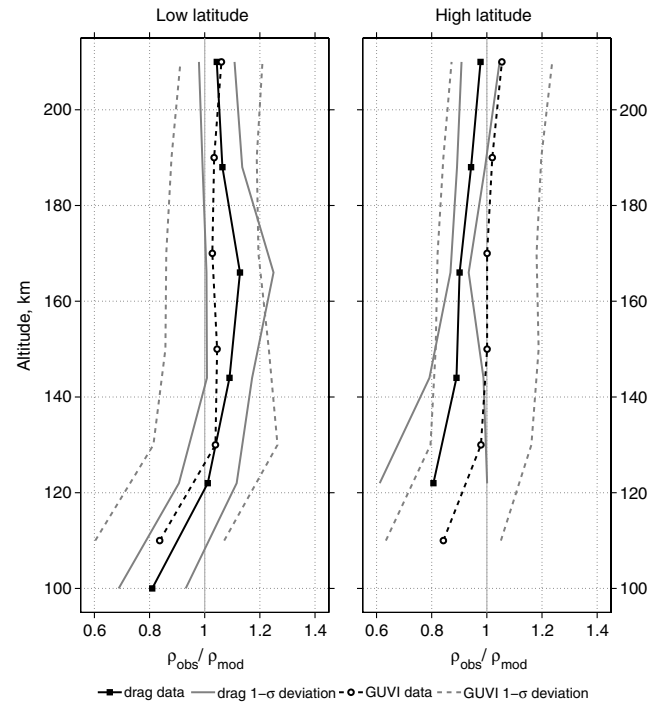

Fig. 16   Ratios of observed and modeled densities for satellite drag and GUVI measurements.

GUVI and Two-Line Element (TLE) densities is exceptionally poor[††]. Figure 16 shows the comparison between GUVI and drag-measured density ratios. The GUVI and drag-derived density ratios are in good agreement near the equator. Both of the datasets reproduce an overestimation of atmospheric density near 110 km by approximately 20%. The difference between average GUVI and drag densities at high latitudes seems to be maintained at approximately 10% across all altitudes. Drag-derived density ratios are reduced by 20% at 120 km, whereas the GUVI ratios are low by approximately 18% at 110-km altitude. It is important to keep in mind that the high-latitude drag data originates only from the SL-6-Molniya orbits and may therefore include idiosyncrasies in modeling the ballistic coefficients of these objects. Nevertheless, the comparisons indicate that 10–20% of the reduction in fitted ballistic coefficients below 150 km may result from atmospheric-model biases at those altitudes. The remaining 30–40% is due to a decrease in C_D associated with the development of a diffuse-shock region in the transition regime [52].

Several measurements of satellite accommodation coefficients exist that are independent of modeled atmospheric density. The first such measurement analysis was performed in 1966 by Moe on data retrieved from the Explorer-VI satellite [18]. Explorer VI flew in a highly eccentric orbit ($e = 0.76$) with a perigee altitude of approximately 260 km. Soon after the orbit and spin decays of Ariel II ($e = 0.07$) at an altitude of 290 km were analyzed by Moe in 1968 and reanalyzed over longer time spans by Imbro et al. in 1975 [20]. Following these American and British satellites Beletsky analyzed the Russian Proton-II satellite ($e = 0.03$) at a perigee altitude of 168 km [19]. Ching et al. [21] also measured accommodation coefficients independently of density models by measuring the lift and drag of the S3-1 satellite then calculating their ratio. Figure 17 shows accommodation contours produced by the SESAM model as a function of atomic-oxygen partial pressure and perigee velocity with paddlewheel measurements and lift-to-drag measurements indicated by black circles. The locations of the four paddlewheel α estimates in Fig. 17 were computed by propagating the orbits of the four satellites using SGP4. Note that Explorer VI sampled a much different region of the P_O-V_r space, and one would thus expect the accommodation to differ significantly from the other satellites. Figure 18 illustrates the

---

[**]Data available online at http://guvi.jhuapl.edu/levels/level2b/limb2/ [retrieved 25 June 2011].

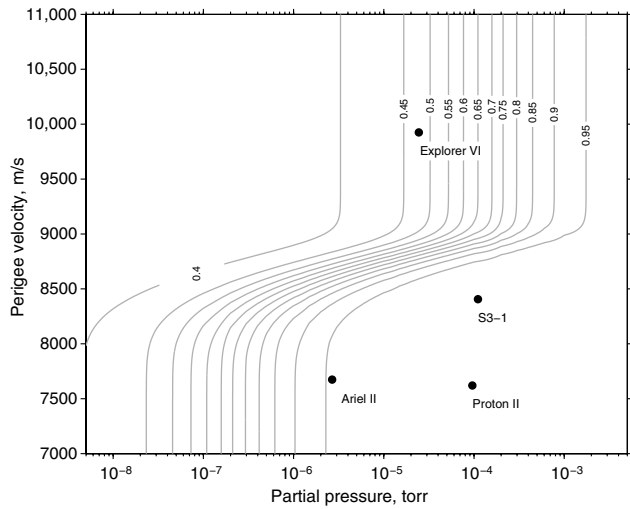[††]Emmert, J. T., personal communication, 8 July 2011.

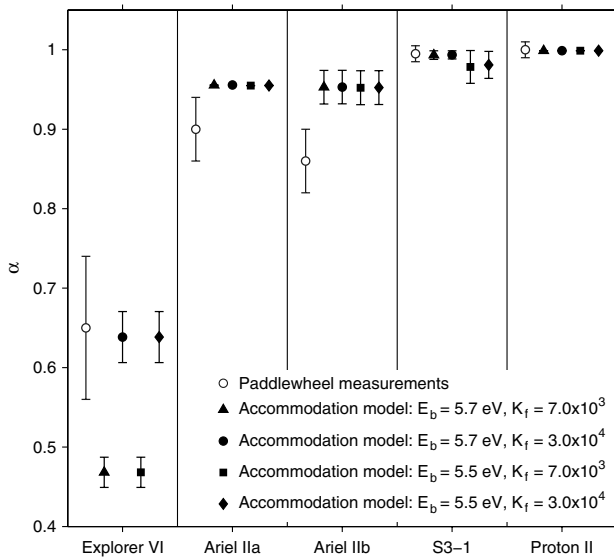**Fig. 17 Energy accommodation as a function of speed and atomic oxygen pressure.**

Fig. 19 Comparison of SESAM accommodation coefficients at different m_s values with independent measurements.

Fig. 18 Comparison of SESAM accommodation coefficients at different $K_{L,f}$ values with independent measurements.

Fig. 20 Comparison of SESAM with fitted data and a model for circular orbits.

direct comparisons between SESAM accommodation coefficients and atmospheric-model-independent measurements. Note that there are two different estimates of Ariel-II results. The first is the result of Moe, analyzed over the first few days of the orbit, and the second is the value obtained by Imbro resulting from the analysis of one month of data [20,53]. Figure 18 displays the SESAM results for several combinations of E_b and $K_{L,f}$ parameters. Recall that $K_{L,f}$ was fixed in the initial determination of model parameters, hence its effect on accommodation should be evaluated. A value of 3.0×10^4 for the $K_{L,f}$ parameter results in the best overall fit with the data, particularly Explorer VI. As for the binding energy E_b 5.7 eV improves the agreement for the S3-1 satellite. Note that SESAM overestimates Ariel-II accommodation data by 5–10%. This discrepancy will motivate future development of the model as well as the pursuit of further atmospheric-model-independent measurements of gas-surface interactions. Figure 19 compares the model results with measurements of accommodation at different values of assumed surface mass m_s. The best agreement results from a surface mass ranging between 60 and 75 amu justifying the default choice of 65 amu in the SESAM model. Figure 20 shows SESAM α compared with accommodation coefficients based on fitted ballistic coefficients [5,22,54] as a function of altitude for average atmospheric conditions. The data shown are based only on near-circular orbits of spherical satellites whose cross-
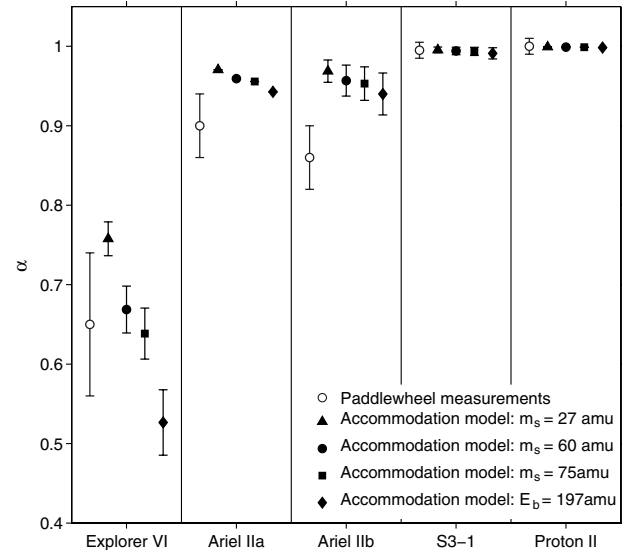
sectional area and mass are known precisely. Results from a previous implementation of a drag-coefficient model based on adsorption of atomic oxygen [4] are shown along with results of the Goodman model. The data and models are separated into solar-minimum and solar-maximum conditions illustrating the effect of space-environment variability on the drag coefficient. Accommodation coefficients at higher altitudes are higher compared with the previous adsorption-based model and compare better with measurements such as the Clementine satellite at 650 km [4,5]. Note the large discrepancy (approximately 40%) between the data and the Goodman model.

Although the average-fixed ballistic model is comparable to SESAM above 200 km, it is not capable of tracking changes in C_D due to changes in accommodation nor due to transition-regime aerodynamics. Furthermore, the average-fixed model cannot be used for an object unless a fitted-ballistic-coefficient time series of several months to several decades already exists for that object. On the other hand SESAM provides a modeling framework for ballistic-coefficient prediction provided that a priori assumptions about the cross-sectional area and mass can be made.

IX.   Conclusions

The fitted ballistic coefficients of 16 spheres and 46 rocket bodies were analyzed at perigee altitudes from 110 to 500 km to construct a ballistic-coefficient model that reconciles the drag observed by various classes of objects. In particular, circular and highly elliptical orbits were included in the dataset as it has been known for over 40 years that the drag coefficient of objects in low Earth orbit may have a strong dependence on velocity. The results of this analysis indicate that the energy accommodation coefficient decreases between 7- and 10-km/s perigee velocities. This transition likely corresponds to a drop in adsorption efficiency of atomic oxygen on satellite surfaces. Attributing this phenomenon to the convolution of freestream kinetic energies with the binding energy of atomic oxygen results in an average binding energy between 5.5 and 5.7 eV, which corresponds well with the average theoretical binding energy for spacecraft materials such as aluminum and Kapton. The observed transition in energy accommodation is fast relative to what would be predicted by modeled temperatures of the atmosphere. This finding is indicative of additional physics that, though captured empirically, are not explicitly included in the semi-empirical model of drag coefficients.

The revised semi-empirical model (SESAM) results in better agreement with observations especially for satellites in elliptical orbits. The agreement between the model and observations was first tested by evaluating the ratio of observed to modeled ballistic coefficients. The ballistic coefficients computed using SESAM resulted in $B_{\mathrm{obs}}/B_{\mathrm{mod}}$ ratios that best approximated a unity mean distribution corresponding to the ratio of two normally distributed random variables with the median located nearest to the mean. Although the improvement over the average-fixed method is marginal above 200 km, the gains are significant below 200-km altitudes with 30–50% improvements in accuracy. This was verified by comparing drag measurements referenced to the SESAM model with remote-sensing observations made by the GUVI instrument. Furthermore, the average-fixed model, which is standard in density measurement analyses based on orbit-averaged drag has no predictive capability for objects that have not been in space long enough for an averaged true ballistic coefficient to be acquired.

There is reasonable agreement between SESAM accommodation coefficients and paddlewheel measurements to within 1–10% with the differences generally being within measurement uncertainties. Furthermore, it is found that an average surface mass adopted for all bodies in the dataset does not result in significant modeling errors owing to the significant levels of atomic-oxygen adsorption. Further comparisons of SESAM results were made with accommodation coefficients estimated through comparison of measured drag to atmospheric models and the differences were within 3% up to 500-km altitudes. There does exist an outlier at 650 km where there is no data on which model construction was based. Also, it is important to note that the outlying data point corresponds to an object that is neither spherical nor randomly tumbling like the rocket bodies. The application of this model is therefore restricted to spherical and randomly tumbling objects flying with arbitrary velocities between 100- and 500-km altitudes.

In addition to the average-fixed model we compared SESAM with models using fixed accommodation coefficients as well as drag coefficients based on the Goodman hard-sphere model of accommodation. The fixed-accommodation model has some precedent in the analysis of accelerometer data, whereas the Goodman model can be successfully applied to reflections of molecules from clean surfaces. Both these models produced large discrepancies in terms of the reduction in altitude-based biases and comparisons with space-based measurements.

Appendix A: Drag Coefficient of a Cylinder

The formulas presented here were derived by Sentman under the assumptions of free-molecular flow and cosine reflection [28]. The equation for the drag coefficient of a cylinder $C_{D,\mathrm{cyl}}$ can be decomposed into the drag coefficient of the cylindrical section $C_{D,\mathrm{side}}$ and that of two end caps $C_{D,\mathrm{cap}\text{-}n}$ (see Fig. A1).

$$C_{D,\mathrm{cyl}} = \frac{[(C_{D,\mathrm{cap}\text{-}a} + C_{D,\mathrm{cap}\text{-}b})\pi d^2/4 + C_{D,\mathrm{side}}ld/2)}{A_{\mathrm{cyl}}} \quad (A1)$$

In Eq. (A1) l and d refer to the length and diameter of the cylinder, respectively. For the cylindrical section the equation is

$$C_{D,\mathrm{cap}\text{-}n} = C_{N,\mathrm{cap}\text{-}n} \sin x + C_{A,\mathrm{cap}\text{-}n} \cos x \quad (A2a)$$

$$\begin{aligned} C_{N,\mathrm{cap}\text{-}n} &= (s \sin x/\sqrt{\pi} + 0.5\sqrt{T_{\mathrm{kin,out}}/T_a}) \exp(-s^2 \sin^2 x)/s^2 \\ &+ [(0.5 + s^2 \sin^2 x) + (0.5\sqrt{T_{\mathrm{kin,out}}/T_a}\sqrt{\pi}s \sin x)] \\ &\cdot [1 + \mathrm{erf}(s \sin x)]/s^2 \end{aligned} \quad (A2b)$$

$$\begin{aligned} C_{A,\mathrm{cap}\text{-}n} &= [(s \cos(x)/\sqrt{\pi})[\exp(-s^2 \sin^2(x)] \\ &+ \sqrt{\pi}s \sin(x)\{1 + \mathrm{erf}[s \sin(x)]\}/s^2 \end{aligned} \quad (A2c)$$

$$x = \begin{cases} \beta & \text{if } n = a, \text{plate}a \\ \beta + \pi & \text{if } n = b, \text{plate}b \end{cases} \quad (A2d)$$

where s is the speed ratio and β is the angle of attack (angle between the freestream velocity vector and the axis of the cylinder). The drag coefficient of the cylindrical side is taken to be

$$C_{D,\mathrm{side}} = C_{N,\mathrm{side}} \sin \beta + C_{A,\mathrm{side}} \cos \beta \quad (A3a)$$

$$\begin{aligned} C_{N,\mathrm{side}} &= s\sqrt{\pi} \sin(\beta)(2\sin^2(\beta) + 1/s^2) \\ &\times \exp\left(-\frac{s^2 \sin^2(\beta)}{2}\right)\left[I_0\left(\frac{s^2 \sin^2(\beta)}{2}\right) + I_1\left(\frac{s^2 \sin^2(\beta)}{2}\right)\right] \\ &+ (2\sqrt{\pi}/s) \sin(\beta) \exp\left(-\frac{s^2 \sin^2(\beta)}{2}\right)I_0\left(\frac{s^2 \sin^2(\beta)}{2}\right) \\ &+ \sqrt{T_{\mathrm{kin,out}}/T_a}[(\pi^{3/2})/(2s)] \sin(\beta) \end{aligned} \quad (A3b)$$

$$\begin{aligned} C_{A,\mathrm{side}} &= 2s\sqrt{\pi}\sin^2(\beta)\cos(\beta)\exp\left(-\frac{s^2 \sin^2(\beta)}{2}\right) \\ &\times \left[I_0\left(\frac{s^2 \sin^2(\beta)}{2}\right) + I_1\left(\frac{s^2 \sin^2(\beta)}{2}\right)\right] \\ &+ (2\sqrt{\pi}/s)\cos(\beta)\exp\left(-\frac{s^2 \sin^2(\beta)}{2}\right)I_0\left(\frac{s^2 \sin^2(\beta)}{2}\right) \end{aligned} \quad (A3c)$$

where I_0 and I_1 are the modified Bessel functions of first kind with degree 0 and 1, respectively. Equations (A4a–A4h) describe the total cross-sectional area of the cylinder.

$$A_{\mathrm{cyl}} = A_{\mathrm{cap}\text{-}a} + A_{\mathrm{cap}\text{-}b} + A_{\mathrm{side}} \quad (A4a)$$
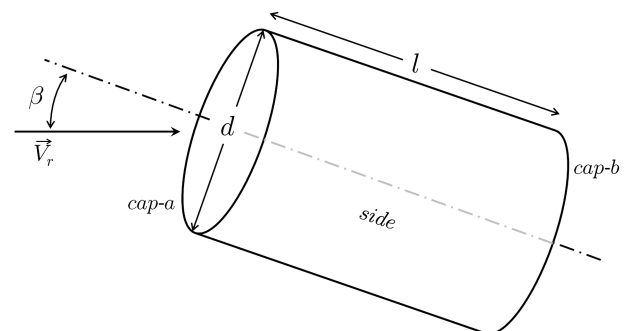
Fig. A1   Cylinder of diameter d and length l flying at angle of attack β.

$$\rho_O, T_a$$

Call to NRLMSISE-00
at satellite location

Based on spacecraft velocity, compute
the Langmuir adsorption parameter

$$E_r = \tfrac{1}{2} m_O \left\| \vec{V}_{sc} - \vec{V}_w \right\|^2$$

$$s_o = f(E_r, E_b, T_{ad}) \quad (\text{equation 26b})$$

$$K_L = s_o K_{L,o} + K_{L,f}$$

Compute atomic-oxygen partial-pressure parameter

$$P_O = \tfrac{1}{2} \rho_O \left\| \vec{V}_{sc} - \vec{V}_w \right\|^2 \left(\tfrac{2s^2+1}{\sqrt{\pi} s^3} \exp(-s^2) \tfrac{4s^4+4s^2+1}{2s^4} \mathrm{erf}(s) \right)$$

$$\bar{m}$$

$$K_L$$

Compute the effective energy
accommodation coefficient

$$\mu = \tfrac{\bar{m}}{m_s}$$

$$\alpha_s = \tfrac{2.4\mu}{(1+\mu)^2}$$

$$\theta' = \tfrac{K_L P_O}{1 + K_L P_O}$$

$$\alpha = (1 - \theta')\alpha_s + \theta'$$

$$P_O$$

$$\alpha$$

Obtain drag coefficient from
lookup table or equation 7

$$C_{D,mod}$$

Calibrate the ballistic coefficient or evaluate
it based on a priori propellant margin

$$m_{obs} = \left\langle \tfrac{C_{D,mod} A}{B_{obs}} \right\rangle_{\Delta t}$$

$$m_{obs} = m_{dry} + \eta_{prop} m_{prop}$$

$$B_{mod} = \tfrac{C_{D,mod}}{m_{obs}}$$

Fig. C1   Implementation of SESAM.

$$A_{\mathrm{cap}\text{-}a} = \frac{\pi d^2 \cos |\beta|}{4} \tag{A4b}$$

$$A_{\mathrm{cap}\text{-}b} = A_{\mathrm{cap}\text{-}a} \quad \text{if} \quad \frac{l \sin |\beta|}{2} \geq \frac{d \cos |\beta|}{2} \tag{A4c}$$

$$A_{\mathrm{cap}\text{-}b} = A_{\mathrm{cap}\text{-}a} - 2(A_{\mathrm{sec}} - A_{\mathrm{tri}}) \quad \text{if} \quad \frac{l \sin |\beta|}{2} < \frac{d \cos |\beta|}{2} \tag{A4d}$$

$$A_{\mathrm{sec}} = \frac{d^2 \cos |\beta|}{4} \{ a \tan[\cos |\beta| \tan(\pi/2)]$$
$$- a \tan(\cos |\beta| \tan\{a \sin[l \sin |\beta|/(d \cos |\beta|)]\}) \} \tag{A4e}$$

$$A_{\mathrm{tri}} = \{[l \sin(|\beta|)/2]/ \tan\{a \sin[l \sin |\beta|/(d \cos |\beta|)]\}\}$$
$$L \sin |\beta|/2 \tag{A4f}$$

$$A_{\mathrm{side}} = ld \sin |\beta| - A_{\mathrm{cap}\text{-}a} \quad \text{if} \quad \frac{l \sin |\beta|}{2} \geq \frac{D \cos |\beta|}{2} \tag{A4g}$$

$$A_{\mathrm{side}} = ld \sin |\beta| - [A_{\mathrm{cap}\text{-}a} - 2(A_{\mathrm{sec}} - A_{\mathrm{tri}})]$$
$$\text{if} \quad \frac{l \sin |\beta|}{2} < \frac{d \cos |\beta|}{2} \tag{A4h}$$

Appendix B: Partial-Pressure Parameter for Spherical and Randomly Tumbling Objects

The partial-pressure parameter is taken by multiplying the partial-acceleration equation Eq. (1) by spacecraft mass and dividing by cross-sectional area. The resulting force-per-area equation is

$$P_O = F_O/A = \frac{1}{2} \rho_O C_{D,\mathrm{in},O} V_r^2 \tag{B1}$$

where ρ_O is the mass density of atomic oxygen and $C_{D,\mathrm{in},O}$ is the drag coefficient for incoming molecules only. The equation for $C_{Di,O}$ is taken to be the equation for the drag coefficient of a sphere with the reflection temperature set to zero. In other words the term $\frac{2\sqrt{\pi}}{3s} \sqrt{T_{\mathrm{kin,out}}/T_a}$ in Eq. (7) is set to zero, and the result is substituted into Eq. (B1).

Appendix C Model Implementation

The SESAM model implementation is illustrated by the block diagram in Fig. C1. Model parameters are listed in Table C1. The

Table C1   Optimal parameters for SESAM

Parameter	Symbol	Value
Adsorption energy	E_b	5.7 eV
Transition temperature	T_{ad}	93 K
Initial Langmuir parameter	$K_{L,o}$	5×10^6 torr^{-1}
Final Langmuir parameter	$K_{L,f}$	3×10^4 torr^{-1}
Average substrate mass	m_s	65 amu

Table C2   DSMC drag-coefficient results for velocities of 7500 m/s

Accommodation	120 km	130 km	140 km	160 km	200 km	225 km	300 km
1.00	1.886	1.963	2.006	2.046	2.087	2.096	2.111
0.86	2.187	2.282	2.316	2.352	2.377	2.381	2.391
0.65	2.407	2.516	2.546	2.559	2.577	2.583	2.590
0.00	2.828	2.909	2.935	2.947	2.961	2.963	2.970

Table C3   DSMC drag-coefficient results for velocities of 10,300 m/s

Accommodation	120 km	130 km	140 km	160 km	200 km	225 km	300 km
1.00	1.871	1.929	1.969	2.006	2.043	2.055	2.070
0.86	2.237	2.308	2.331	2.346	2.358	2.361	2.365
0.65	2.449	2.519	2.541	2.551	2.564	2.563	2.568
0.00	2.848	2.914	2.923	2.935	2.946	2.949	2.957

results of direct-simulation Monte-Carlo runs for a 1.6-m-diameter sphere flying in Earth's thermosphere are shown here in Tables C2 and C3. These results form the basis of SESAM lookup tables.

Acknowledgments

References

[1] Bowman, B. R., and Hrncir, S., "Drag Coefficient Variability at 100–300 km from the Orbit Decay Analyses of Rocket Bodies," *American Astronautical Society/AIAA Astrodynamics Specialist Conference*, AIAA, Univelt, Inc., San Diego, CA, 2007; also AAS Paper 2007-262.

[2] Moe, K., Moe, M. M., and Wallace, S. D., "Improved Satellite Drag Coefficient Calculations from Orbital Measurements of Energy Accomodation," *Journal of Spacecraft and Rockets*, Vol. 35, No. 3, 1998, pp. 266–272.
doi:10.2514/2.3350

[3] Dogra, V. K., Wilmoth, R. G., and Moss, J. N., "Aerothermodynamics of a 1.6-Meter-Diameter Sphere in Hypersonic Flow," *AIAA Journal*, Vol. 30, No. 7, 1992, pp. 1789–1794.
doi:10.2514/3.11137

[4] Pilinski, M. D., Argrow, B. M., and Palo, S. E., "Semi-Empirical Model for Satellite Energy-Accommodation Coefficients," *Journal of Spacecraft and Rockets*, Vol. 47, No. 6, 2010, pp. 951–956.
doi:10.2514/1.49330

[5] Pardini, C., Anselmo, L., Moe, K., and Moe, M., "Drag and Energy Accommodation Coefficients During Sunspot Maximum," *Advances in Space Research*, Vol. 45, No. 5, 2010, pp. 638–650.
doi:10.1016/j.asr.2009.08.034

[6] Moe, K., and Moe, M., "Gas-Surface Interactions and the Satellite Drag Coefficients," *Planetary and Space Science*, Vol. 53, No. 8, 2005, pp. 793–801.
doi:10.1016/j.pss.2005.03.005

[7] Picone, J. M., Emmert, J. T., and Lean, J. L., "Thermospheric Densities Derived from Spacecraft Orbits: Accurate Processing of Two-Line Element Sets," *Journal of Geophysical Research*, Vol. 110, No. A03301, 2002.
doi:10.1029/2004JA010585

[8] Cook, G. E., "Satellite Drag Coefficients," *Planetary and Space Science*, Vol. 13, No. 10, 1965, pp. 929–946.
doi:10.1016/0032-0633(65)90150-9

[9] Reiter, G. S., and Moe, K., "Surface-Particle-Interaction Measurements Using Paddlewheel Satellites," *Rarefied Gas Dynamics*, edited by Wachman, H. Y., Vol. 6, *Rarefied Gas Dynamics, Proceedings of the Sixth International Symposium*, Boston, Academic Press, New York, NY, 1968, pp. 6–20.

[10] Bowman, B. R., and Moe, K., "Drag Coefficient Variability at 175–500 km from the Orbit Decay Analyses of Spheres," *American Astronautical Society/AIAA Astrodynamics Specialist Conference*, American Astronautical Society/AIAA, AAS Publications, San Diego, CA, 2005; also AAS Paper 2005-257.

[11] Gregory, J. C., and Peters, P. N., "A Measurement of the Angular Distribution of 5 eV Atomic Oxygen Scattered Off a Solid Surface in Earth Orbit," *Rarefied Gas Dynamics*, edited by Boffi, Vinicio, and Cercignani, Carlo, Vol. 15, *Proceedings of International Symposium*, B.G. Teubner, Stuttgart, Germany, 1987, pp. 644–656.

[12] Schaaf, S. A., and Chambre, P. L., *Flow of Rarefied Gases*, Princeton Univ. Press, Princeton, NJ, 1961, p. 9.

[13] Engstrom, J. R., Bonser, D. J., Nelson, M. M., and Engel, T., "The Reaction of Atomic Oxygen with Si(100) and Si(111)," *Surface Science*, Vol. 256, No. 3, 1991, pp. 317–343.
doi:10.1016/0039-6028(91)90875-S

[14] Trost, J., Brune, H., Wintterlin, J., Behm, R. J., and Ertl, G., "Interaction of Oxygen with Al(111) at Elevated Temperatures," *The Journal of Chemical Physics*, Vol. 108, No. 4, 1998, pp. 146–150.
doi:10.1063/1.475546

[15] Lee, C., and Chen, L. W., "Reactive Probability of Atomic Oxygen with Material Surfaces in Low Earth Orbit," *Journal of Spacecraft and Rockets*, Vol. 37, No. 2, 2000, pp. 252–256.
doi:10.2514/2.3553

[16] Błoński, P., Kiejna, A., and Hafner, J., "Theoretical Study of Oxygen Adsorption at the Fe(110) and (100) Surfaces," *Surface Science*, Vol. 590, No. 1, 2005, pp. 88–100.
doi:10.1016/j.susc.2005.06.011

[17] Chen, L. W., and Lee, C. H., "Interaction Potential Between Atomic Oxygen and Polymer Surfaces in Low Earth Orbit," *Journal of Spacecraft and Rockets*, Vol. 43, No. 3, 2006, pp. 487–496.
doi:10.2514/1.13373

[18] Moe, K., "Absolute Atmospheric Densities Determined from the Spin and Orbit Decays of Explorer VI," *Planetary and Space Science*, Vol. 14, No. 11, 1966, pp. 1065–1075.
doi:10.1016/0032-0633(66)90022-5

[19] Beletsky, V. V., "An Estimate of the Character of the Interaction Between the Airstream and a Satellite," *Kosmicheskie Issledovaniya*, Vol. 8, No. 10, 1970, pp. 206–217 (in Russian).

[20] Imbro, D. R., Moe, M. M., and Moe, K., "On Fundamental Problems in the Deduction of Atmospheric Densities from Satellite Drag," *Journal of Geophysical Research*, Vol. 80, No. 22, 1975, pp. 3077–3086.
doi:10.1029/JA080i022p03077

[21] Ching, B. K., Hickman, D. R., and Straus, J. M., "Effects of Atmospheric Winds and Aerodynamic Lift on the Inclination of the Orbit of the S3-1 Satellite," *Journal of Geophysical Research*, Vol. 82, No. 10, 1977, pp. 1471–1480.
doi:10.1029/JA082i010p01474

[22] Moe, K., and Bowman, B. R., "The Effects of Surface Composition and Treatment on Drag Coefficients of Spherical Satellites," *American Astronautical Society/AIAA Astrodynamics Specialist Conference*, American Astronautical Society/AIAA, Reston, VA, AAS Publications, San Diego, CA, 2005; also Paper AAS-05-258.

[23] Goodman, F. O., "Thermal Accommodation," *Progress in Surface Science*, Vol. 5, 1974, pp. 261–375.
doi:10.1016/0079-6816(74)90005-7

[24] Goodman, F. O., "A Three-Dimensional Hard Spheres Theory of Scattering of Gas Atoms from a Solid Surface," NASA TR-NASA-CR-933, 1967.

[25] Feibelman, P. J., "The First Wetting Layer on a Solid," *Physics Today*, Vol. 63, No. 2, 2010, pp. 34–39.
doi:10.1063/1.3326987

[26] Biggs, G. A., and Phillips, L. F., "BET Analysis of Thermal Accommodation Coefficients Obtained via Measurements of the Onsager Heat of Transport," *Chemical Physics Letters*, Vol. 452, Nos. 1–3, 2008, pp. 84–88.
doi:10.1016/j.cplett.2007.12.030

[27] Schamberg, R., "Analytic Representation of Surface Interaction For Free Molecule Flow with Application to Drag of Various Bodies," The RAND Corp. TR-R-339, Santa Monica, CA, 1959; also *PROJECT RAND, Aerodynamics of the Upper Atmosphere*, compiled by Masson, D. J.

[28] Sentman, L. H., "Free Molecule Flow Theory and its Application to the Determination of Aerodynamic Forces," Lockheed Missiles and Space Co. TR-LMSC-448514, Armed Services Technical Information Agency, VA, 1961.

[29] Bird, G. A., *Molecular Gas Dynamics and the Direct Simulation of Gas Flows*, Oxford Science Publ., New York, 1994, pp. 172, 40–41, 70, and 77–78.

[30] Pilinski, M. D., Argrow, B. M., and Palo, S. E., "Drag Coefficients of Satellites with Concave Geometries: Comparing Models and Observations," *Journal of Spacecraft and Rockets*, Vol. 48, No. 2, 2011, pp. 312–325.
doi:10.2514/1.50915

[31] Sutton, E., "Normalized Force Coefficients for Satellites with Elongated Shapes," *Journal of Spacecraft and Rockets*, Vol. 46, No. 1, 2009, pp. 112–116.
doi:10.2514/1.40940

[32] Doornbos, E., Forster, M., van Helleputte, T., van den IJssel, J., Koppenwallner, G., Luhr, H., Rees, D., and Visser, P., "Air Density Models Derived from Multi-Satellite Drag Observations," European Space Agency Study CR TR-21022/07/NL/HE, Delft, The Netherlands, 2009.

[33] Bird, G. A., "Sophisticated DSMC," *Direct-Simulation-Monte-Carlo 2007 Meeting*, Santa Fe, NM, Sept. 2007, http://www.ae.su.oz.au/dsmc_gab/Resources/DSMC07notes.pdf.

[34] Boahnhardt, H., Koehnke, H., and Seidel, A., "The Acceleration and the Deceleration of the Tumbling Period of Rocket Intercosmos 11 During the First Two Years After Launch," *Astrophysics and Space Science*, Vol. 162, No. 2, 1989, pp. 297–313.
doi:10.1007/BF00640745

[35] Pontieu, B. D., "Database of Photometric Periods of Artificial Satellites," *Advances in Space Research*, Vol. 19, No. 2, 1997, pp. 229–232.
doi:10.1016/S0273-1177(97)00005-7

[36] Reynolds, R., Jost, J., Rubin, G., and Vila, J., "Radar Measurements of the Reentry of the Ariane 504 EPC," *Advances in Space Research*, Vol. 28, No. 9, 200l, pp. 1269–1275.
doi:10.1016/S0273-1177(01)00396-9

[37] Storz, M. F., Bowman, B. R., Branson, J. I., and Casali, S. J., "High Accuracy Satellite Drag Model (HASDM)," *Advances in Space Research*, Vol. 36, No. 12, 2005, pp. 2497–2505.
doi:10.1016/j.asr.2004.02.020

[38] Bowman, B. R., and Storz, M. F., "High Accuracy Satellite Drag Model (HASDM) Review," *2003 AAS/AIAA Astrodynamics Specialist Conference*, Advances in the Astronautical Sciences, Vol. 116, Univelt, Inc., San Diego, CA, 2003.

[39] Bowman, B. R., and Tobiska, W. K., "Improvements in Modeling Thermospheric Densities Using New EUV and FUV Solar Indices," *American Astronautical Society/AIAA Astrodynamics Specialist Conference*, American Astronautical Society, Univelt, Inc., San Diego, CA, 2006; also Paper No. 06-237.

[40] Bowman, B. R., "True Satellite Ballistic Coefficient Determination for HASDM," *AIAA/American Astronautical Society Astrodynamics Specialist Conference and Exhibit*, Monterey, CA, AAS Publications, San Diego, CA, 2002; also Paper No. 4887.

[41] Isakowitz, S. J., Hopkins, J. B., and Hopkins, J. P. Jr., *International Reference Guide to Space Launch Systems*, AIAA, Reston, Virginia, 1999, pp. 14–28, 192–203, and 383–385.

[42] Vallado, D. A., Crawford, P., Hujsak, R., and Kelso, T. S., "Revisiting Spacetrack Report 3: Rev 1," AIAA Paper No. 2006-6753-Rev1, 2006.

[43] Tapley, B. D., Schutz, B. E., and Born, G. H., *Statistical Orbit Determination*, Elsevier, New York, 2004, p. 31.

[44] Oura, K., Liftshits, V. G., Saranin, A. A., Zotov, A. V., and Katayama, M., *Surface Science*, Springer–Verlag, Berlin, 2003, pp. 296–306.

[45] Kay, B. D., and Coltrin, M. E., "Quantum Tunneling and the Activated Chemisorption of Methane on Tungsten," *Surface Science Letters*, Vol. 198, No. 3, 1988, pp. 375–379.
doi:10.1016/0039-6028(88)90368-8

[46] Błoński, P., Kiejna, A., and Hafner, J., "Oxygen Adsorption on the Clean and O-precovered Fe (110) and (100) Surfaces," *Journal of Physics: Condensed Matter*, Vol. 19, No. 9, 2007, pp. 1–8.
doi:10.1088/0953-8984/19/9/096011

[47] Baker, T. A., Friend, C. M., and Kaxiras, E., "Atomic Oxygen Adsorption on Au(111) Surfaces with Defects," *Journal of Physical Chemistry*, Vol. 113, No. 8, 2009, pp. 3232–3238.
doi:10.1021/jp806952z

[48] Emmert, J. T., "A Long-Term data Set of Globally Averaged Thermospheric Total Mass Density," *Journal of Geophysical Research*, Vol. 114, No. A06315, 2009.
doi:10.1029/2009JA014102

[49] Paxton, L. J., "GUVI: A Hyperspectral Imager for Geospace," *Proceedings of Society of Photo-Optical Instrumentation Engineers*, Vol. 5660, SPIE, Bellingham, WA, 2004, pp. 228–240.

[50] Emmert, J. T., Meier, R. R., Lean, J. L., and Christensen, A. B., "Thermospheric Density 2002-2004: TIMED/GUVI Dayside Limb Observations and Satellite Drag," *Journal of Geophysical Research*, Vol. 111, No. A10S16, 2006.
doi:10.1029/2005JA011495

[51] Meier, R. R., and Picone, J. M., "Retrieval of Absolute Thermospheric Concentrations from the Far UV Dayglow: An Application of Discrete Inverse Theory," *Journal of Geophysics Research*, Vol. 99, No. A4, 1994, pp. 6307–6320.
doi:10.1029/93JA02775

[52] Koppenwallner, G., and Legge, H., "Drag of Bodies in Rarefied Hypersonic Flow," *Thermophysical Aspects of Re-Entry Flows*, AIAA, 1985; also Paper No. 85-0998.

[53] Moe, K., "Recent Experimental Evidence Bearing on Satellite Drag Coefficients," *AIAA Journal*, Vol. 6, No. 7, 1968, pp. 1375–1377.
doi:10.2514/3.4754

[54] Moe, M. M., Wallace, S. D., and Moe, K., "Recommended Drag Coefficients for Aeronomic Satellites," *Geophysical Monograph*, Vol. 87, 1995, pp. 349–445.
doi:10.1029/GM087

I. Boyd
Associate Editor